Titre: Title:	Scattering in Space-Time Abruptly Modulated Structures
Auteur: Author:	Zoé-Lise Deck-Léger
Date:	2017
Type:	Mémoire ou thèse / Dissertation or Thesis
Référence: Citation:	Deck-Léger, Z.-L. (2017). Scattering in Space-Time Abruptly Modulated Structures [Mémoire de maîtrise, École Polytechnique de Montréal]. PolyPublie. https://publications.polymtl.ca/2565/

URL de PolyPublie: PolyPublie URL:	https://publications.polymtl.ca/2565/
Directeurs de recherche: Advisors:	Christophe Caloz
Programme: Program:	génie électrique

UNIVERSITÉ DE MONTRÉAL

SCATTERING IN SPACE-TIME ABRUPTLY MODULATED STRUCTURES

ZOÉ-LISE DECK-LÉGER
DÉPARTEMENT DE GÉNIE ÉLECTRIQUE
ÉCOLE POLYTECHNIQUE DE MONTRÉAL

MÉMOIRE PRÉSENTÉ EN VUE DE L'OBTENTION
DU DIPLÔME DE MAÎTRISE ÈS SCIENCES APPLIQUÉES
(GÉNIE ÉLECTRIQUE)
AVRIL 2017

UNIVERSITÉ DE MONTRÉAL

ÉCOLE POLYTECHNIQUE DE MONTRÉAL

Ce mémoire intitulé:

SCATTERING IN SPACE-TIME ABRUPTLY MODULATED STRUCTURES

présenté par: DECK-LÉGER Zoé-Lise
en vue de l'obtention du diplôme de: Maîtrise ès sciences appliquées
a été dûment accepté par le jury d'examen constitué de:

M. AKYEL Cevdet, D.Sc.A., président
M. CALOZ Christophe, Ph. D., membre et directeur de recherche
M. SKOROBOGATIY Maksim, Ph. D., membre

ACKNOWLEDGEMENTS

I would like to thank Christophe Caloz for integrating me to his team, and for suggesting the topic of modulated space-time structures. I very much enjoyed studying this topic, which proved to be very vast, with many unexplored and interesting problems. I thank him for this great opportunity, for the guidance and the contagious enthusiasm.

Mohammed Salem contributed to this work in many ways, in particular by developing an original method to solve temporal crystals. I am grateful for all the time he spent teaching and guiding me in this work. Walid Dyab uncovered important works in the litterature of space-time media, and clarified the difference between moving media and modulated media. I thank him for this thorough work and the time we spent studying seminal works of this field. Maksim Skorobogatiy brought the topic of inverse Doppler effect to our attention, and his input was very valuable. Thanks also to Nima, Karim and Dr. Zou for the discussions and insightful input.

I would also like to thank Rhanem for the encouragement, especially at the start when I needed it the most, Christian for his help with some mathematical developments, Catherine for the discussions about research in general and Hussein for the advice about writing.

RÉSUMÉ

Cette thèse propose une contribution originale à l'étude de la propagation d'ondes électromagnétiques dans des structures modulées spatio-temporellement. Les structures modulées ont été abondamment étudiées, d'abord pour les circuits radio-fréquences et par la suite en optique, et il existe aujourd'hui plusieurs dispositifs modulés pour diverses applications.

Habituellement, ces structures sont modulées avec une onde ayant une vitesse de modulation sousluminale. Dans ce travail, on s'attarde plutôt à étudier des structures dont la vitesse de modulation est superluminale. Ces structures superluminales ne contredisent pas la théorie de la relativité restreinte, car la modulation est transverse à la direction de propagation de l'onde. Ces structures ont été très peu étudiées, et elles présentent pourtant des propriétés fondamentales très intéressantes, qui seront l'objet principal de ce mémoire.

Dans une première partie, on présente une méthode diagrammatique pour résoudre des structures modulées, ou spatio-temporelles (ST). On représente des structures ST dans le diagramme de Minkowski et dans le diagramme de dispersion avec les transformations de Lorentz.

Dans la seconde partie, on s'attarde à résoudre un bloc superluminal, en calculant les propriétés des ondes transmises et réfléchies. En comparant les résultats obtenus avec ceux d'un bloc sousluminal, on constate que les solutions sont symétriques. Les fréquences, les angles de déflection et les amplitudes sont symétriques pour des vitesses opposées.

Dans la troisième partie, une succession périodique de blocs superluminaux, qu'on nomme cristal superluminal, est étudié. On propose une méthode pour calculer les ondes transmises et réfléchies pour un cristal de durée finie. On détermine les conditions d'interférence pour une période dans un cristal. Cela nous permet de déduire les zones d'instabilités. Les résultats sont validés numériquement par la méthode des différences finies dans le domaine du temps, mieux connue sous l'acronyme anglais FDTD.

Finalement, deux structures périodiques modulées sont présentées ; la première structure est un cristal sousluminal qui compresse une onde après une réflexion. La deuxième structure est un cristal stationnaire terminé par un mur en mouvement. Il est connu que l'effet Doppler inverse a lieu dans cette structure, et nous utilisons notre méthode diagrammatique pour le montrer.

ABSTRACT

In this thesis, we explore the scattering of electromagnetic waves from Space-Time Modulated (STM) structures, and provide a general method to represent and solve such structures.

First, we present a diagrammatic method used throughout the thesis to solve STM structures. This diagrammatic method borrows tools from special relativity; the Minkowski diagram and Lorentz transformations. We solve four half-space modulation problems, corresponding to spatial, subluminal, temporal and superluminal modulations.

Next a superluminal slab is solved diagrammatically and mathematically. A symmetry between waves scattered from subluminal and superluminal problems is uncovered.

Third, we solve a succession of superluminal slabs, which we refer to as superluminal crystals. We use a method radically different from the standard Bloch-Floquet approach: the fields scattered from one slab are the incident waves for the next slab, therefore the results of each interface are cascaded. This method would *not* be applicable to subluminal crystals, because in that case there are multiple reflections in each slab. For superluminal crystals, there are no such reflections, and so the problem is actually *simpler* than the subluminal counterpart.

Finally, we present two more periodic STM structures. The first is a subluminal crystal that is shown to compress waves after reflection. The second is a stationary crystal bounded by a moving wall that is known to give rise to the inverse Doppler effect. The inverse Doppler effect is explained diagrammatically, to provide additional insight.

TABLE OF CONTENTS

LIST OF FIGURES

LIST OF APPENDICES

CHAPTER 1 INTRODUCTION

The propagation of waves in inhomogeneous structures is a very mature field. Fundamental problems of scattering from a dielectric were solved in the early seventeenth century, with works by Fresnel, Kepler, Snell and Descartes leading to the development of optical instruments such as lenses. Periodic dielectric structures were later addressed by Lord Rayleigh (Strutt, 1887), and extended to three dimensions by Yablonovitch (1987). These were shown to give rise to bandgaps, which enabled the moulding of light.

The addition of time variation to these spatial inhomogeneities gives an additional degree of freedom to control waves. In particular, it leads to frequency changes, which do not occur in time-invariant media. Structures that are inhomogeneous in space and time are usually called modulated structures. These structures have a rich history, starting with microwave structures such as travelling-wave parametric amplifiers (Cullen, 1958; Tien, 1958), and later optical structures, in particular acousto-optics and nonlinear media (Saleh and Teich, 2007).

Modulated structures, that are both space- and time-invariant, are the focus of this thesis. In this work they are called Space-Time Modulated (STM). We use this terminology since in this work, we classify space-time inhomogeneous structures according to space and time dependence. This classification sheds light on unexplored problems. For instance, any inhomogeneous stationary structure, with a refractive index varying in space $n(z)$, has a corresponding temporally-varying problem $n(t)$. Although inhomogeneous structures have been studied in great detail, very little work has been done on temporally-varying structures, studies being limited to half-space problems or periodic structures. Also, structures modulated at subluminal velocities, which have a refractive index function of space and time, $n(z - vt)$, have a corresponding superluminal problem, obtained by inverting the time and space dependance, $n(t - vz)$. Superluminal modulation does *not* contradict the special theory of relativity if the modulation is transverse to the direction of propagation of the wave. An explanation of how this is achieved will be provided. The subluminal problems are much more present in the literature than their symmetric superluminal counterpart. The tools used for inhomogeneous stationary structures or subluminal modulation can be adapted to solve the temporal or superluminal counterpart. This is the main focus of the work presented here.

We will limit our study to *abrupt*, linearly moving STM structures. By abrupt, we mean subcycle: smaller than the spatial wavelength or temporal period of the incident wave. By linear motion, we mean that we do not address accelerating media. Although we limit ourselves

to a few problems, our general classification of STM structures leads us to identify many unsolved problems that will keep us busy for years to come.

1.1 Historical Milestones

Many important works on STM were solved in the 1970s. We limit the literature review of this time period to constant-velocity motion of single discontinuities, slabs, and periodic media.

Subluminal moving slabs were first solved by Yeh and Casey (1966). Subluminal modulated discontinuities were later solved by Kunz (1980). Moving modulation is *not* equivalent to a moving structure, as in the moving structure, Fizeau drag is induced (Fizeau, 1851). Kunz clearly makes this distinction in his paper. Both papers solved the problems by using Lorentz transformations to apply boundary conditions in a frame where the interface seems at rest.

Temporal discontinuities, consisting of an instantaneous modulation everywhere in space, were first solved by Morgenthaler (1958), who applyed continuity conditions at the temporal interface between media. The study was extended to dispersive structures by Felsen and Whitman (1970), using Green's function and introducing a diagrammatic method to solve such problems. The diagrammatic method we will present generalizes his approach. Fante (1971) later solved a time-varying dielectric half-space, instead of the infinite varying time step of the previous works.

Periodic subluminal STM problems were solved by Cassedy and Oliner (1963), Tamir and Wang (1966) and Chu and Tamir (1969), with Tamir and Wang (1966) including an oblique incidence analysis, and using isofrequency diagrams to determine the direction of the different harmonics. All these works were based on a generalized Bloch-Floquet approach. The periodic superluminal STM problem was solved by Cassedy (1967), who noted instabilities arising in this type of media.

Concerning the feasibility of such devices, Holberg and Kunz (1966) suggested a temporal modulation could be realized using ferrite-loaded waveguides, and Pierce (1958) modeled superluminal modulation on transmission lines.

1.2 Recent Research

More recently, many advances have been made in STM structures: new problems were solved and many new applications were proposed, most notably the use of the intrinsic non-reciprocity of STM media.

1.2.1 Nonreciprocity and Isolation

Yu and Fan (2009) were the first, to our knowledge, to note that isolation could be achieved in STM media. Magnetless nonreciprocity was then proposed by Sounas et al. (2013), creating a Faraday rotation by applying a rotational modulation. Estep et al. (2014) realized a magnetless circulator based on modulated coupled-resonator loops. Chamanara et al. (2016) proposed an optical isolator based on asymmetric photonic bandgaps, associated with an STM periodic structure. A duplexer antenna operating differently in transmission and reception, based on a periodic STM structure, was proposed by Taravati and Caloz (2017). A time-varying metasurface was shown to induce non-reciprocity in (Shaltout et al., 2015).

1.2.2 STM Structures

Some recent theoretical works addressed new fundamental problems. A vibrating crystal was studied in (Skorobogatiy and Joannopoulos, 2000a,b), and the band structure was derived and interband transitions were calculated. Biancalana et al. (2007) solved ST discontinuities using a symmetric version of Maxwell's equations, and provided the frequencies and amplitudes of the scattered waves for normal incidence. Zurita-Sánchez et al. (2009) solved a spatially finite temporal crystal, using Bloch-Floquet theory and mode matching. Salem and Caloz (2015) solved a temporal crystal by cascading successive temporal slabs, noting that no reflections occur in time. This work inspired the solution of the superluminal slab in this thesis. An ST checkerboard was introduced in (Lurie and Weekes, 2006; Lurie and Yakolev, 2016) and solved numerically. It was shown that certain checkerboard geometries lead to focusing of a wave and energy accumulation.

1.2.3 Miscellaneous ST Effects

Finally, ST structures were shown to exhibit a great variety of interesting effects, such as Doppler reversal, temporal cloaking, and real-time time reversal.

The inverse Doppler effect, consisting of the opposite trend of the Doppler effect (approaching objects create a downshift) was shown to occur in periodic transmission lines in (Seddon and Bearpark, 2003). The same effect was observed in a photonic crystal (Reed et al., 2003). Ran et al. (2015) experimentally realized a tunable transmission line which can operate as a left-handed or a right-handed line. When the transmission line is left-handed, the inverse Doppler effect is observed, while the right-handed transmission line leads to the standard Doppler effect.

Temporal cloaking, a dual problem to spatial cloaking, was introduced in (McCall et al., 2011)

and experimentally realized in (Fridman et al., 2012) using phasers, or chirping elements. The idea is to cloak an event, rather than cloak a position in space. The event cloaking is based on dispersion, whereas diffraction is used for spatial cloaking.

Real-time time reversal occurs at temporal interfaces. This was shown experimentally with water waves in (Bacot et al., 2016). Water waves are launched in a pool. A sudden jerk is applied to the pool, to create a temporal discontinuity. The waves are seen to refocus back to the original launching point. (Sivan and Pendry, 2011) suggested time reversal could also be realized in zero-gap periodic systems.

1.3 Motivation

As the litterature review suggests, after a significant interest for STM structures in the 1960s-70s, there was a relatively calm period with few developments in this area. There is presently a renewal of interest, possibly due to the emergence of metamaterial studies. Indeed metamaterials, which are three-dimensional engineered structures, can achieve a great diversity of wave transformations. Engineering four-dimensional structures with inhomogeneities in space and time enables even more diversity of wave manipulation. Another incentive to study these structures is the inherent nonreciprocity of STM structures, therefore replacing magnets in nonreciprocal structures.

Our main motivation for studying STM structures is therefore to gain additional control on the scattering of waves. Another motivation is the existence of the fundamental unsolved problems. By solving these unexplored problems, we hope to find related novel phenomena, and develop new applications.

1.4 Description of the Work

This thesis solves the scattering of electromagnetic waves from a few fundamental STM problems. The work is organized as follows.

Chapter 2 first represents STM structures in the Minkowski diagram. In this representation, the spatial and temporal variations are drawn, and can have any arbitrary dependence. Linear-motion STM media are then solved diagrammatically by combining Lorentz transformations and Minkowski and dispersion diagrams. Four categories of half-spaces are solved: a spatial half-space, a subluminal one, a temporal half-space, corresponding to an instantaneous change, and a superluminal half-space.

This diagrammatic method is then applied to solve a superluminal slab in Chapter 3. The

superluminal slab is also mathematically solved, for the case of an oblique incident wave. A symmetry between the scattering from subluminal and superluminal slabs is shown to exist.

A superluminal crystal is addressed in Chapter 4. This is studied as a succession of superluminal slabs. This crystal is shown to have amplification regions, and these regions are localized on the dispersion diagram. An interferometric explanation, extending Bragg law to moving structures, is provided.

Chapter 5 then presents two miscellaneous topics: a subluminal crystal is shown to realize ST focusing in reflection, and the inverse Doppler effect in periodic media is solved diagrammatically. The ST focusing idea was inspired by works on dispersion compensation, which is usually realized in transmission. It exploits the nonreciprocity that is inherent to STM structures. The inverse Doppler effect is explained diagrammatically.

1.5 Contributions

This thesis presents a few original works. The first contribution is the diagrammatic approach, that systematically solves linear-motion problems. The second contribution is the resolution of the scattering from a superluminal slab, presented in section 3.1. The third contribution is the new symmetry observed between the scattering from subluminal and superluminal slabs: it is shown that the reflected angles and the temporal frequencies are the same for slabs having opposite velocities. This is described in section 3.2. Finally, a novel explanation of the position of the instability points in superluminal crystal diagrams is given in section 5.2, and the inverse Doppler effect is demonstrated diagrammatically in section 5.2.

CHAPTER 2 DIAGRAMMATIC APPROACH

This chapter presents a diagrammatic method to represent and solve STM structures. It first introduces the Minkowski diagram, in which waves and STM structures are represented. It then solves four types of STM discontinuities.

2.1 Waves in Minkowski and Dispersion Diagrams

Minkowski (1909) introduced a space-time diagram, the Minkowski diagram, to visualize special relativity. The Minkowski diagram combines space and time quantities on a cartesian graph with vertical and horizontal axes corresponding to space $\mathbf{r}$ and time t. A point in the Minkowski diagram corresponds to an event, at a given location and a given time. Two simultaneous events occurring at time t_0 are depicted in Fig. 2.1(a). A line in the diagram corresponds to a trajectory, also called world line. Constant slopes correspond to constant velocities, as the slope of a trajectory is inversely proportional to its velocity. Fig. 2.1(b) shows trajectories with subluminal ($v < c$) and superluminal ($v > c$) constant velocities, represented as lines with slopes greater or smaller than the light line, $v = c$, which has a slope of 1. A decelerating trajectory is presented in Fig. 2.1(c): the velocity, maximal at time $t = 0$, progressively slows down to 0.

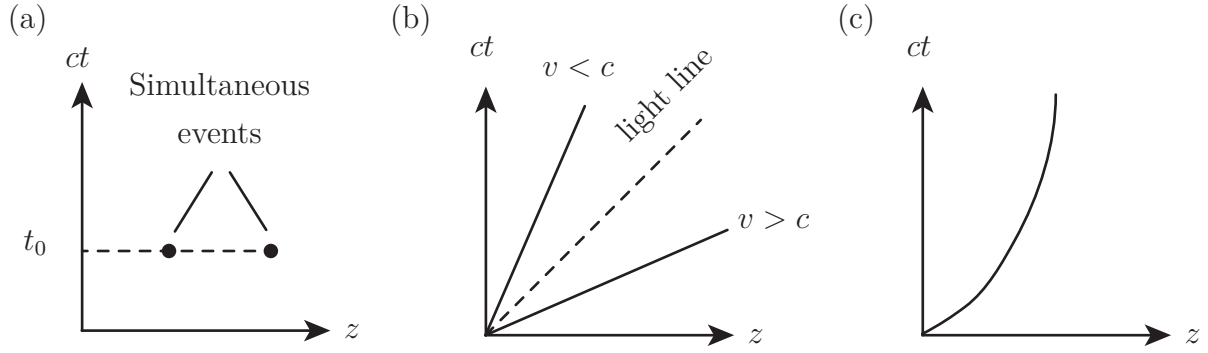

Figure 2.1 Minkowski diagram. (a) Two simultaneous events. (b) Subluminal, superluminal trajectories. (c) Deceleration.

Figure 2.2 (a) illustrates a harmonic wave $\psi(z,t) = e^{i(k_1 z - \omega_1 t)}$ propagating in the z direction in a medium with refractive index n_1. The grey lines represent the trajectories of the crests.

The wavelength λ_1 and the period T_1 of the wave are found geometrically by taking the projections on the space and time axes.

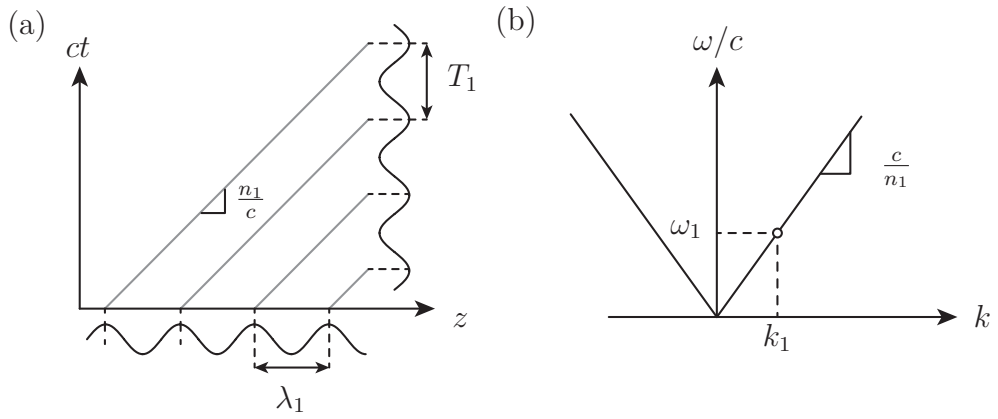

Figure 2.2 Representations of harmonic wave $\psi(z,t) = e^{i(k_1 z - \omega_1 t)}$. (a) Minkowski diagram. (b) Dispersion diagram.

The associated dispersion diagram, representing the inverse space-time, $\mathbf{k} - \omega$, is presented in Fig. 2.2(b). The dispersion diagram of the medium is drawn with slope $v = c/n_1$. The space-time frequencies $\omega_1 = 2\pi/T_1$ and $k_1 = 2\pi/\lambda_1$ are shown.

A 3D dispersion diagram is illustrated in Fig. 2.3(a). A harmonic plane wave $\psi(x,z,t) = e^{i(k_{x1}x + k_{z1}z - \omega_1 t)}$ propagating in x and z is represented as a red dot. In order to work with 2D diagrams, this 3D diagram is projected on two planes. One plane cuts the cone at $k_x = k_{x1}$, and the other at $\omega = \omega_1$. The intersections are drawn in Figs. 2.3(b) and (c), corresponding to the dispersion diagram and the isofrequency diagram. The direction of the group velocity $v_\mathrm{g} = \nabla_\mathbf{k}\omega$ is found geometrically by taking the normal to the isofrequency curve.

2.2 Lorentz Transformation in Minkowski and Dispersion Diagrams

Lorentz transformations relate quantities measured in frames moving at a constant velocities with respect to each other. The Lorentz transformations for space and time are mathematically expressed as:

$$z' = \gamma\left(z - \beta ct\right), \qquad ct' = \gamma\left(ct - \beta z\right) \tag{2.1}$$

with $\gamma = 1/\sqrt{1-\beta}$ and $\beta = v/c$, where z', t' correspond to the space-time quantities measured in a frame moving with velocity v, and z, t correspond to the rest frame quantities. We want to draw the axes of the moving frame (z', ct') onto the Minkowski diagram whose axes

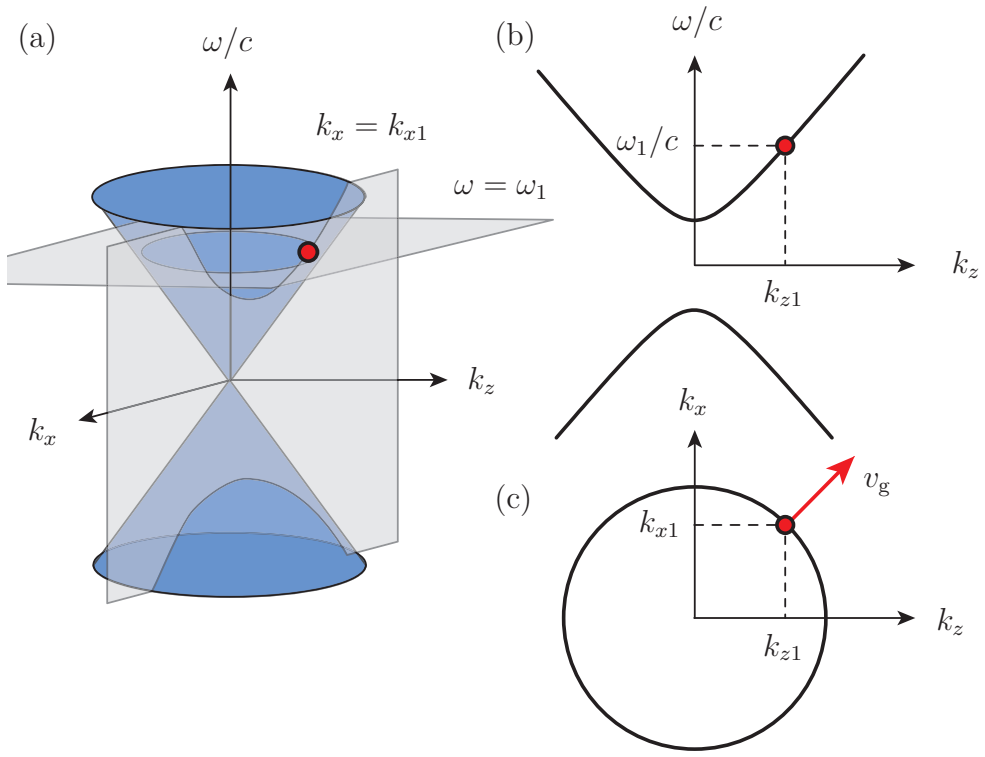

Figure 2.3 Dispersion diagrams for oblique incidence. (a) Dispersion cone with plane cuts at constant k_{x1} and ω_1. (b) Corresponding dispersion diagram (axis $\omega - k_z$). (c) Corresponding isofrequency diagram (axis $k_x - k_z$).

are (z, ct). The z' axis corresponds to the condition $ct' = 0$. From (2.1), we find

$$ct' = \gamma\,(ct - \beta z) = 0, \quad \longrightarrow \quad ct = \beta z, \tag{2.2}$$

and so the slope of the z' axis is $ct/z = \beta$. Similarly, the ct' axis, corresponding to $z' = 0$ is found as

$$z' = \gamma\,(z - \beta ct) = 0 \quad \longrightarrow \quad ct = \frac{1}{\beta} z, \tag{2.3}$$

such that the slope is $ct/z = 1/\beta$. Plotting these axes on the Minkowski diagram in Fig. 2.4, we find the moving frame axes form a skewed cartesian coordinate system. We also see that two events can seem simultaneous in the moving frame, but appear at different times in the rest frame.

The Lorentz transformations for space-time frequencies (ω, k_z) are (Jackson, 1975):

$$k_z' = \gamma\left(k_z - \beta\frac{\omega}{c}\right), \qquad \frac{\omega'}{c} = \gamma\left(\frac{\omega}{c} - \beta k_z\right). \tag{2.4}$$

The transformations are the same, and therefore the superposition of moving and stationary frames will be identical, as seen in Fig. 2.4(b). Isofrequency lines in the moving frame are parallel to the k'_z axis. In the figure, two waves appear to have the same frequency in the moving frame, but have different frequencies in the rest frame.

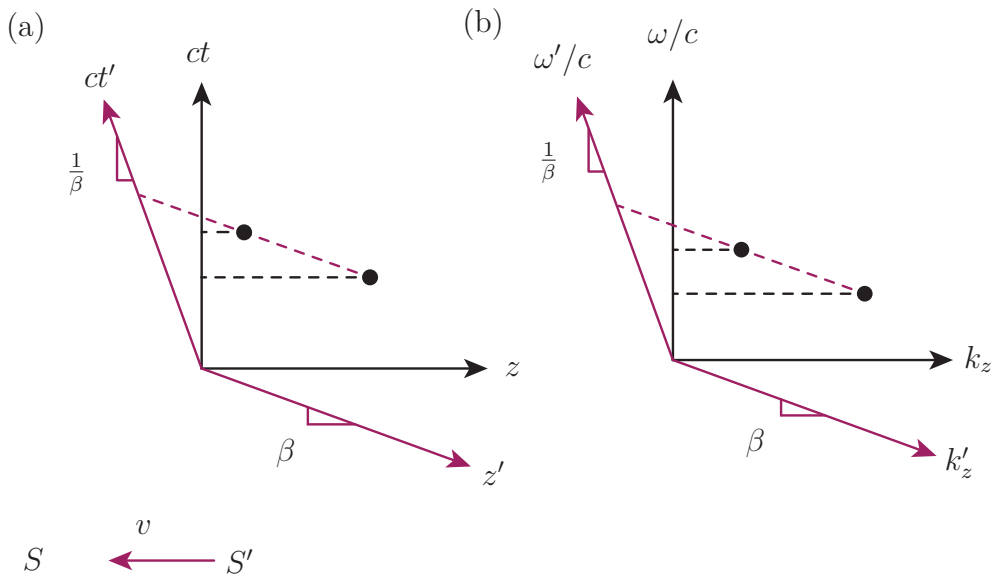

Figure 2.4 Lorentz transform relating frame S to frame S'. (a) Direct space. (b) Inverse space.

2.3 STM Structures in the Minkowski Diagram

STM structures are conveniently represented in the Minkowksi diagram. Fig. 2.5 illustrates the diversity of STM structures by providing some examples. The white and grey zones correspond to media with refractive indices n_1 and n_2. The first row of Fig. 2.5 includes a slab, a lozenge, a circle, and an irregular structure. These structures expand and then compress back, in the two first cases at linear velocity, and for the other two by decelerating and accelerating. The second row includes periodic structures: a succession of STM slabs, which we refer to as STM crystal, a checkerboard, studied in (Lurie and Yakolev, 2016), a succession of crescents and a checkerboard made of irregular shapes.

2.4 Classification of STM Discontinuities

In this thesis, we limit our study to STM structures that are abruptly modulated: the structures consist of only two refractive indices, and there are no intermediate refractive index

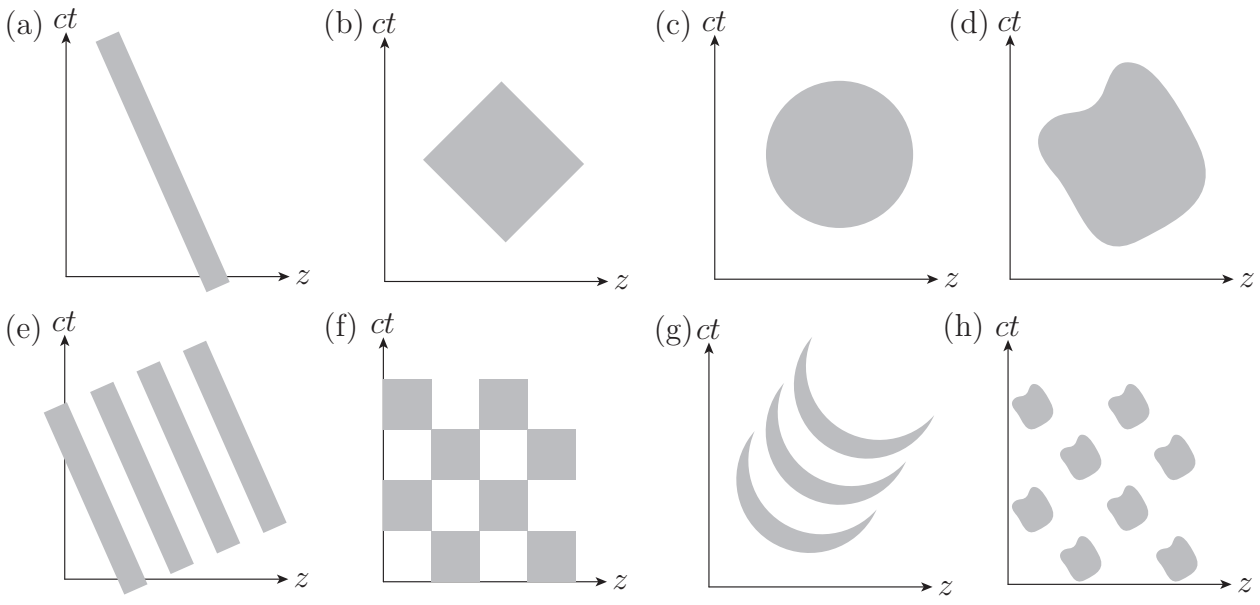

Figure 2.5 STM structure examples. (a) Slab. (b) Lozenge. (c) Circle. (d) Irregular shape. (e) Crystal. (f) Checkerboard. (g) Periodic Crescents. (h) Checkerboard of irregular shape.

values. The interfaces or discontinuities that constitute these structures may be classified according to their modulation velocity, v_{m}, using Minkowski diagrams, as shown in Fig. 2.6 for the case of discontinuity in the z-direction. In these diagrams, ψ_{i}, ψ_{r} and ψ_{t} represent the trajectories of incident, reflected and transmitted waves, respectively. In all four cases, there exists a mathematical solution that is unphysical because it is going back in time, and is therefore acausal. This solution is indicated with an X.

Fig. 2.6(a) presents a *spatial* interface in the Minkowski diagram as a vertical line at z_0 parallel to the ct axis separating two media of refractive indices n_1, n_2. The reflected wave ψ_{r} is in the same medium as the incident wave.

A *subluminal* interface, Fig. 2.6(b), is an interface propagating at a subluminal velocity. It is represented as an oblique line having a slope greater than 1, corresponding to $|v_{\mathrm{s}}|/c < 1$. The reflected wave ψ_{r} is in the same medium as the incident wave. The spatial interface is a limiting case of a subluminal interface with $v = 0$.

A *temporal* interface, Fig. 2.6(c), appears everywhere in space at a given time t_0. It is represented as a horizontal line parallel to the z axis. Both waves scattered from this type of slab emerge in medium 2.

A *superluminal* interface, Fig. 2.6(d), is an oblique line with a slope less than 1, corresponding

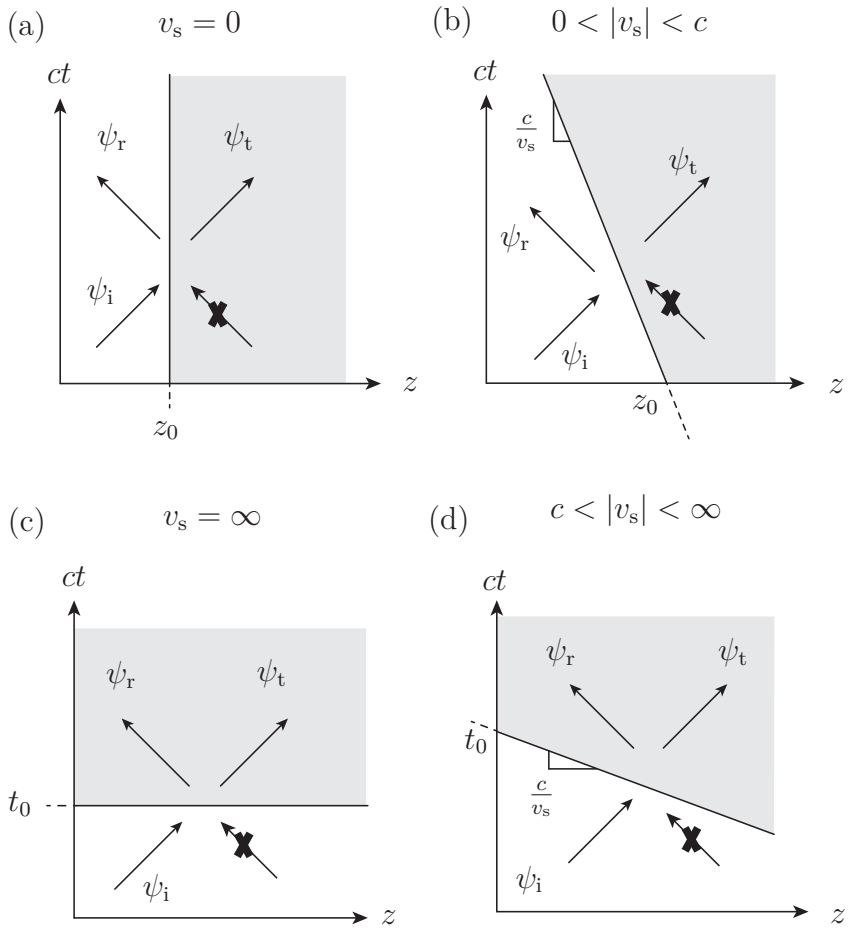

Figure 2.6 Classification of space-time modulated (STM) discontinuities in terms of their velocity, v_s, relative to the velocity of light c. (a) Spatial. (b) Subluminal, approaching. (c) Temporal. (d) Superluminal, approaching.

to $|v_s|/c > 1$. As for the temporal slab case, both scattered waves $\psi_{r,t}$ emerge in the second medium. The temporal interface is a limiting case of the subluminal interface with $v = \infty$.

2.5 Realizing Superluminal Modulation

As stated in the introduction, it is possible to realize superluminal modulation by using tranverse modulation. Here we explain how this is possible.

A common example of superluminality is the superluminal motion of the vertex of two subluminal scissor blades. Fig. 2.7(a) provides an illustration. Suppose a scissor with a stationary blade and a blade moving downwards at velocity $v_b = c$, where c is the speed of light. There is no rotation, only translation. In this case, the velocity of the vertex v_v is seen to be greater

than the velocity of the blade, and thus superluminal.

An analogous circuital realization is presented in Fig. 2.7(b). A pulse generator is connected to seven different sections of a nonlinear transmission line. When the pulse reaches the line, the refractive index changes due to the nonlinearity of the line. The circuit is designed such that the rightmost element has the shortest path, and is activated first. The other paths are incrementally longer. The signal on each path is propagating at $v_s = c$. The velocity of modulation v_m is seen to be greater than the velocity of the signals v_s. Temporal modulation, presented in Fig. 2.6(c), can be realized if all the lines have the same length: the modulation then appears everywhere on the line at a given instant in time.

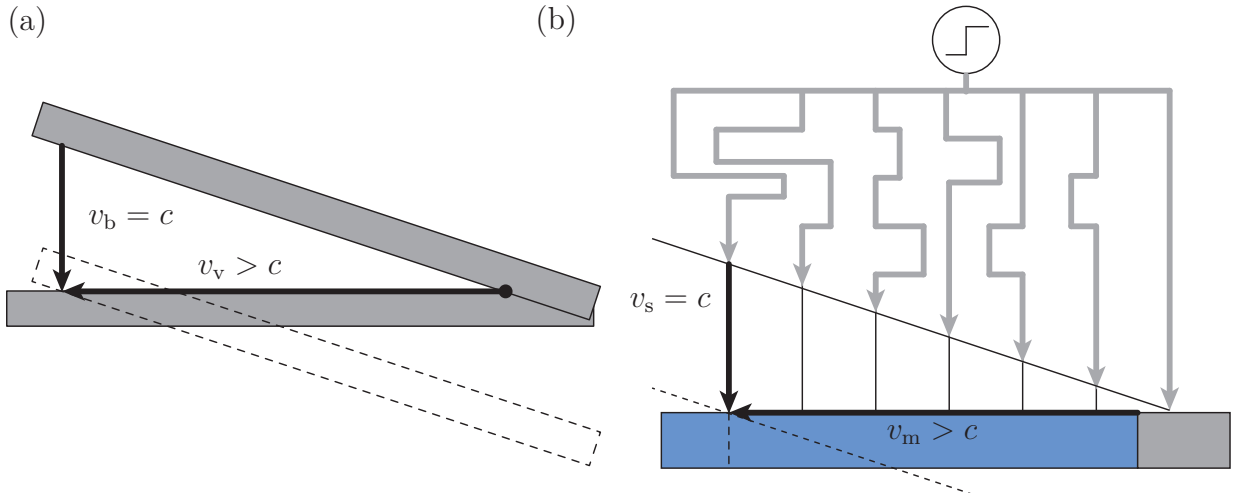

Figure 2.7 Transverse modulation leading to superluminal modulation. (a) Superluminal scissors. (b) Superluminal modulation in transmission line.

2.6 Diagrammatic Method Applied to STM Discontinuities

Combining the representation of waves and structures in the Minkowski diagram and the reciprocal dispersion diagram, we now proceed to solve the scattering of a wave from STM discontinuities, or interfaces, corresponding to Fig. 2.6. We will refer to the Minkowski space as the direct space, and the reciprocal space-time frequency space as the inverse space.

2.6.1 Spatial Discontinuity

We first address the ubiquitous problem of a spatial discontinuity. Figure 2.8(a) illustrates the scattering of a pulse incident on a spatial discontinuity in the Minkowski diagram. It is

constructed as follows: 1) Draw the STM structure. 2) Plot the trajectory of the incident pulse. 3) Plot the trajectory of the reflected and the transmitted pulse, knowing that the pulse is immediately scattered at the interface: it suffers no delay. The slopes of the trajectories are proportional to the refractive index, and so the trajectory of the transmitted wave is steeper. An acausal solution, a wave scattered into the second medium and propagating backwards in time, is discarded.

The duration and the spatial extent of the waves are found by taking vertical and horizontal projections. We find the the three waves have the same duration Δt, and the transmitted pulse has a smaller waist than the incident and reflected pulses.

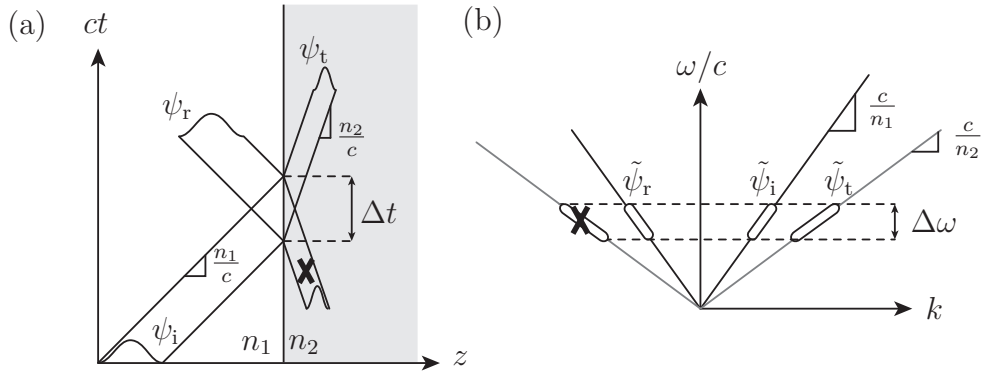

Figure 2.8 Pulse scattering from spatial discontinuity. (a) Minkowski Diagram (direct space). (b) Dispersion diagram (inverse space).

Figure 2.8(b) illustrates the corresponding dispersion diagram. It is constructed as follows: 1) Draw the dispersion diagram for both media. 2) Locate the incident wave spectrum $\tilde{\psi}_i$. 3) Trace the isofrequency lines parallel to the k axis. 4) Locate the solutions, at the intersection of the isofrequency and the dispersion curves. The reflected wave is propagating in $-z$ direction, with $k_z < 0$, and the transmitted field is propagating in $+z$ direction, with $k_z > 0$. The reflected field is in medium 1 and the transmitted field is in medium 2. The acausal solution, corresponding to a backward wave ($k_z < 0$) in the second medium, is discarded.

Consistently with our observation in the direct space, where we noted the temporal duration of the waves was conserved, in the inverse space the temporal frequencies are conserved. Also, the transmitted pulse has a greater k_z than the incident pulse, which corresponds to a smaller waist in the direct space.

2.6.2 Subluminal Discontinuity

We now slove the problem of an approaching discontinuity. Figure 2.9(a) illustrates the scattering problem in the Minkowski diagram. The incident pulse ψ_i scatters into a reflected ψ_r and a transmitted ψ_t wave at the discontinuity. A frame moving at the same velocity as the discontinuity sees a stationary slab, and therefore the time axis ct' of this moving frame is parallel to the discontinuity. We observe from this diagram that the duration of the waves is conserved in the moving frame, $\Delta ct' = 0$. The waist of the reflected wave ψ_r is shorter than the incident wave. Taking a vertical cut, the temporal duration of the reflected wave is also seen to be shorter than the incident wave. This effect is the Doppler effect.

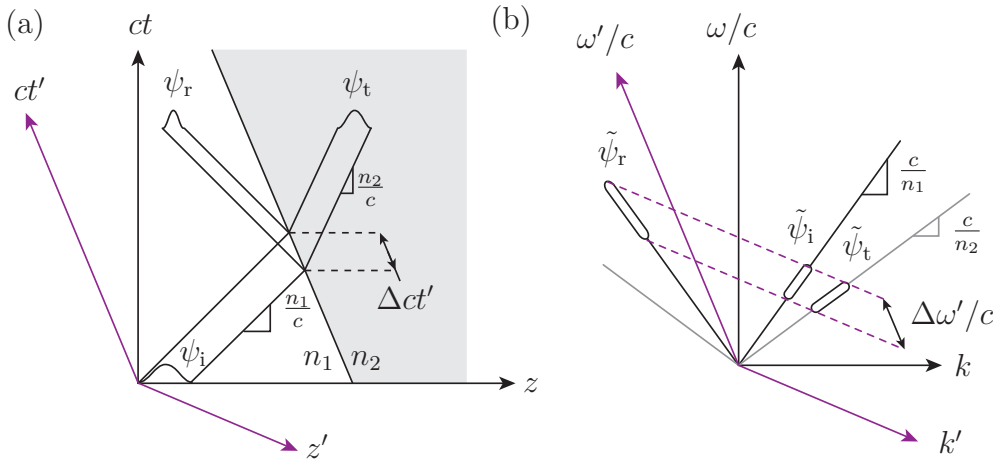

Figure 2.9 Pulse scattering from subluminal discontinuity. (a) Minkowski diagram. (b) Dispersion diagram.

Figure 2.9(b) illustrates the corresponding dispersion diagram, with stationary and moving frame axes. The slab appears stationary in the moving frame, and therefore the temporal frequencies are conserved in this frame ($\omega'_\mathrm{i} = \omega'_\mathrm{r,t}$). The diagram is constructed following steps similar to the case of a spatial discontinuity: 1) Draw the dispersion diagram for both media. 2) Draw the axes of the moving frame. 3) Locate the incident wave spectrum. 4) Trace the isofrequency lines parallel to the k' axis, corresponding to frequency conservation ω'/c. 5) Locate the solutions, at the intersection of the isofrequency and the dispersion curves.

Note that the slopes of the dispersion curves are unaffected by the modulation. The modulation does not affect the group velocity of the waves. The picture would be different if the medium was actually in motion, as in that case the velocities in the forward and backward directions would be different, due to Fizeau drag.

The frequency of the reflected wave is higher than that of the incident wave in the stationary

frame, as predicted by Doppler for an approaching discontinuity.

2.6.3 Temporal Discontinuity

The dual problem of the spatial discontinuity, a temporal discontinuity, is solved in Fig. 2.10. The diagrammatic solution for this problem was proposed by Felsen and Whitman (1970) for the more general case of dispersive media.

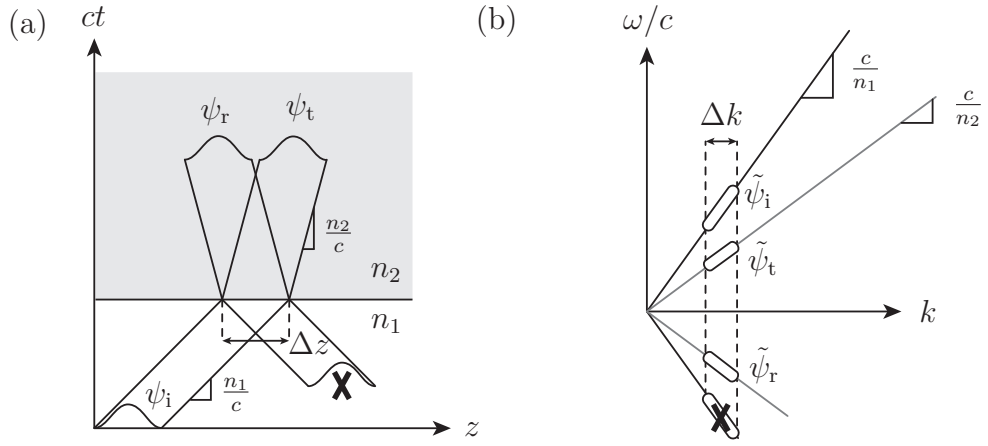

Figure 2.10 Pulse scattering from temporal discontinuity. (a) Minkowski diagram (b) Dispersion diagram.

Figure 2.10 (a) represents the scattering of the incident wave ψ_i into a reflected ψ_r and a transmitted ψ_t wave in the Minkowski diagram. The spatial waist Δz of the waves is conserved, since there is no drift along the interface. The temporal duration of the scattered pulses is greater than that of the incident wave.

We noticed the spatial waist of the waves is conserved, and so the spatial frequencies (k_z) are conserved at a temporal interface. The dispersion diagram solution, Fig. 2.10 (b), is obtained in a dual manner to the spatial problem: the dispersion diagram is drawn, the incident field is located, and the spatial isofrequency, corresponding to lines parallel to the ω/c axis, is drawn. Note the reflected wave has negative temporal frequencies. This is the dual of the spatial case, where negative spatial frequencies were obtained for the reflected wave. Negative frequencies can be shown to correspond to phase conjugation, or time reversal, and an experimental realization of this was presented by Bacot et al. (2016) for acoustic waves. The acausal solution in this problem is the backward wave propagating in medium 1.

2.6.4 Superluminal Discontinuity

Finally, we solve the problem of a superluminal discontinuity. A solution for superluminal discontinuities is provided in (Biancalana et al., 2007), using a symmetric expression of Maxwell's equations. Our contribution is to suggest a diagrammatic solution, which provides more insight into the problem, and to solve the problem by using Lorentz transformation and solving the problem in a moving frame in which the interface appears to have an infinite velocity.

Let us first naively draw the scattering of a wave from a superluminal interface in Fig 2.11(a) based on the sole fact that the waves are instantly scattered from the interface and knowing the velocity of the waves before and after the interface. Drawing this picture, we find that the reflected wave is in the second medium, as is the case for the scattering from a temporal interface, since it is slower than the interface.

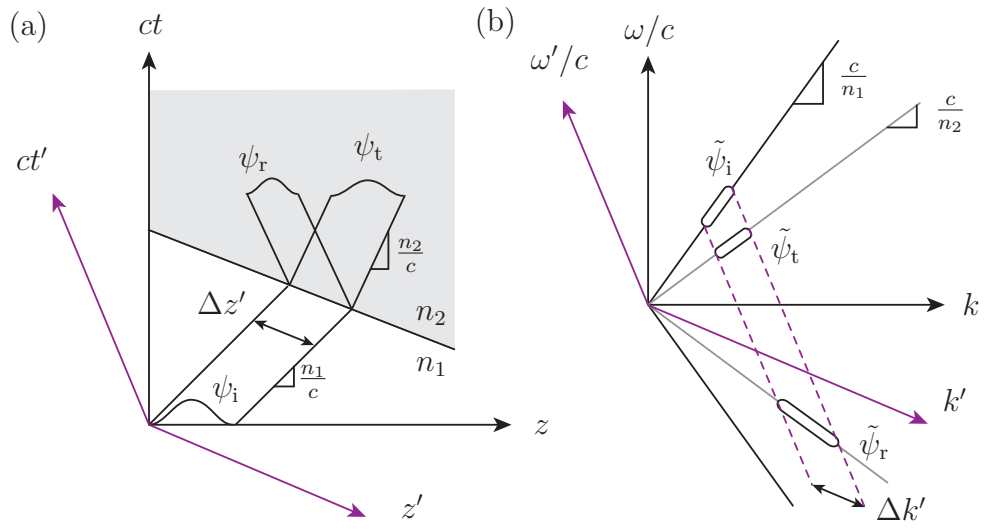

Figure 2.11 Pulse scattering from superluminal discontinuity. (a) Minkowski diagram. (b) Dispersion diagram.

Contrarily to the subluminal discontinuity problem, we *cannot* solve the superluminal discontinuity problem in a frame moving at the same velocity as the discontinuity, for this would yield complex ST quantities. Indeed, recalling the Lorentz transformation for space and time:

$$z' = \gamma\left(z - \beta ct\right), \qquad ct' = \gamma\left(ct - \beta z\right) \tag{2.5}$$

with $\gamma = 1/\sqrt{1-\beta}$ and $\beta = v/c$, we immediately see that $v > c \;\rightarrow\; \beta > 1$ would yield a complex γ and therefore complex z' and ct' quantities. We suggest instead to solve the

superluminal discontinuity problem in a frame of reference in which the discontinuity appears to be temporal, corresponding to the z' axis parallel to the interface, as shown in Fig. 2.11(a).

This moving frame is *not* moving at a superluminal speed. It is moving at a velocity inversely proportional to the velocity of the discontinuity ($v_{\mathrm{mf}} \propto 1/v_{\mathrm{m}}$) where v_{mf} is the velocity of the moving frame and v_{m} is the velocity of the modulation. This can be demonstrated mathematically using the relativistic addition of velocities formula:

$$v_{\mathrm{m}} = \frac{v'_{\mathrm{m}} + v_{\mathrm{mf}}}{1 + \frac{v'_{\mathrm{m}} v_{\mathrm{mf}}}{c^2}} \tag{2.6}$$

with v_{m} and v'_{m} the velocities of the slab as seen in the rest and in the moving frame, respectively. The velocity of the slab as seen in the moving frame is infinite: $v_{\mathrm{m}} = \infty$, and therefore (2.6) becomes

$$v_{\mathrm{m}} = \frac{c^2}{v_{\mathrm{mf}}}. \tag{2.7}$$

The velocities are inversely proportional, which is what we wanted to demonstrate.

In the moving frame, the discontinuity appears temporal, and therefore the spatial frequencies are conserved ($k_{\mathrm{i}}{}' = k_{\mathrm{r,t}}{}'$). The dispersion diagram solution of Fig. 2.11 (b) is obtained in a dual manner to the subluminal problem: the dispersion diagram is drawn, with moving and stationary frame axes, the incident field is located, and the spatial isofrequency, corresponding to lines parallel to the ω'/c axis, are drawn. As for the temporal discontinuity case, the reflected wave has negative temporal frequencies. The reflected wave has a higher frequency than the transmitted wave, which is consistent with the observation of the pulse durations in the direct space-time diagram.

2.7 Conclusion

Four types of STM interfaces were solved diagrammatically. The contribution of this chapter was the solution of the superluminal interface. It was accomplished by going in a frame in which the interface appeared temporal, and applying the continuity conditions of temporal interfaces in this frame. The next chapter extends this work by solving a superluminal slab made of two superluminal interfaces, and considering the case of normal incidence. The coefficients are also derived mathematically.

CHAPTER 3 SUPERLUMINAL STM SLABS

In this chapter, we solve the scattering of a wave from a superluminal slab. Biancalana et al. (2007) solved a superluminal interface problem for normal incident waves. We extend this work by solving a slab, instead of a single interface, and calculating the case of oblique incidence. The method we use to solve a slab is inspired by the work of Salem and Caloz (2015), who had a similar procedure to solve temporal slabs. Our first contribution is therefore to extend the previous works and completely solve a superluminal slab. Our second contribution is to uncover a symmetry in the scattering properties of sub- and super-luminal slabs. This symmetry was found from the diagrammatic method. The following is an adaptation and an expansion of (Deck-Léger and Caloz, 2016).

3.1 Scattering from Superluminal Space-Time Slabs

We restrict ourselves to the problem of a y-polarized wave propagating in the xz-plane incident on a superluminal slab of width D moving in the z direction. The problem is illustrated in Fig. 3.1. As noted in section 2.6.4, the scattered waves at the first interface both scatter into the second medium, since the reflected wave is slower than the interface of the medium, and so it cannot escape. We now add a second interface, and both scattered waves emerge in the third medium. The goal in this section is to calculate the amplitudes, frequencies and direction of these scattered waves.

The fields before, inside and after the superluminal slab may be written as

$$\mathbf{E}_m^{\pm} = A_m^{\pm} e^{i(k_{xm}^{\pm} x + k_{zm}^{\pm} z \mp \omega_m^{\pm} t)} \hat{\mathbf{y}}, \tag{3.1a}$$

where the subscript m denotes the medium ($m = 1, 2, 3$) and the superscripts $+$ and $-$ indicate forward and backward propagation, respectively. Inserting (3.1a) into Maxwell-Faraday equation yields

$$\mathbf{B}_m^{\pm} = \mp A_m^{\pm} \frac{n_m}{c} e^{i(k_{xm}^{\pm} x + k_{zm}^{\pm} z \mp \omega_m^{\pm} t)} \left(\cos\theta_m^{\pm} \hat{\mathbf{x}} - \sin\theta_m^{\pm} \hat{\mathbf{z}} \right), \tag{3.1b}$$

where we defined the wavenumbers

$$k_{zm}^{\pm} = k_m^{\pm} \cos\theta_m^{\pm}, \qquad k_{xm}^{\pm} = k_m^{\pm} \sin\theta_m^{\pm}, \qquad k_m^{\pm} = \omega_m^{\pm} n_m / c, \tag{3.1c}$$

where n_m is the refractive index of medium m and $\theta_m^{\pm}$ is the propagation angle defined from

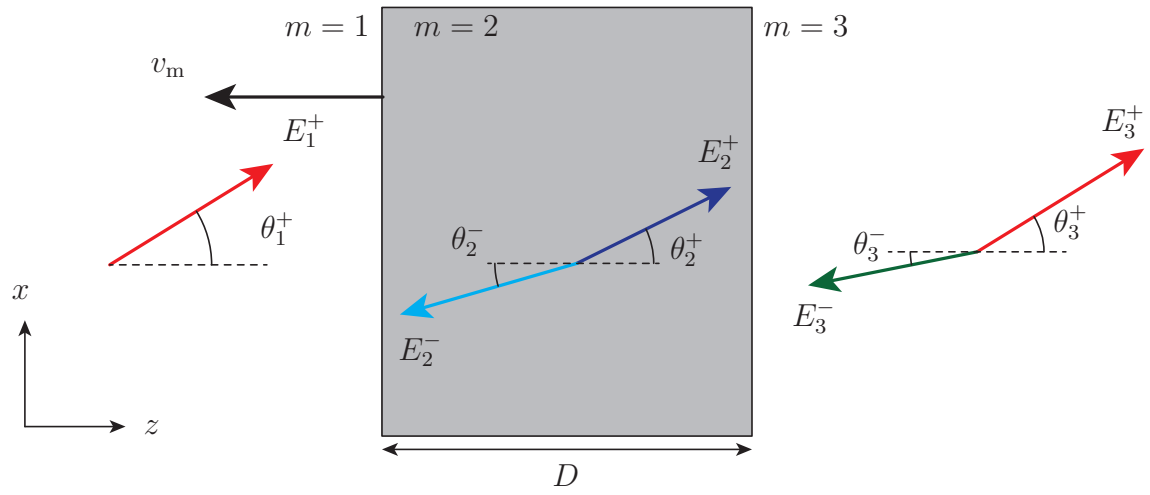

Figure 3.1 Definitions of the fields incident on and scattered from a superluminal slab.

the normal to the interface. Assuming that the media are isotropic, dispersionless, linear, and homogeneous, the constitutive relations in each region read

$$\mathbf{D}_m^\pm = \epsilon_m \mathbf{E}_m^\pm, \qquad \mathbf{B}_m^\pm = \mu_m \mathbf{H}_m^\pm, \tag{3.1d}$$

with permittivity ϵ_m and permeability μ_m. There is an ongoing controversy, the Abraham-Minkowski controversy, concerning what quantities are conserved at a temporal interface. Morgenthaler (1958) suggested that the **D** and **B** fields are continuous at a temporal interface, contrarily to spatial interfaces, where continuity concerns the **E** and **H** fields. We will suppose this to be true, and proceed with the derivations. The methodology would be similar if this were found to be the wrong choice. Therefore at a superluminal interface, we suppose these fields are continuous in the moving frame, i.e.

$$\left[\mathbf{D}'_m = \mathbf{D}'_{m+1}\right]_{t'=0}, \quad \left[\mathbf{B}'_m = \mathbf{B}'_{m+1}\right]_{t'=0}. \tag{3.2}$$

In order to solve (3.2), the fields (3.1) are expressed in the moving frame using Lorentz transformations (Rothwell and Cloud, 2009):

$$c\mathbf{D}'_\perp = \gamma\left(c\mathbf{D}_\perp + \boldsymbol{\beta} \times \mathbf{H}_\perp\right), \quad c\mathbf{B}'_\perp = \gamma\left(c\mathbf{B}_\perp - \boldsymbol{\beta} \times \mathbf{E}_\perp\right). \tag{3.3}$$

Where, since the motion is only in the z direction, $\boldsymbol{\beta} = \beta\hat{\mathbf{z}}$, with β previously defined as $\beta = v_\mathrm{mf}/c = c/v_\mathrm{s}$ (see section 2.6.4) and where $\gamma = 1/\sqrt{1-\beta^2}$. The Lorentz transformations

in the z direction for a y-polarized wave propagating in the xz-plane reduce to:

$$cD'_y = \gamma\left(cD_y + \beta H_x\right), \qquad cB'_x = \gamma\left(cB_x + \beta E_y\right), \qquad cB'_z = cB_z. \tag{3.4}$$

Inserting (3.4) into (3.2) for the interface between media $m = 1$ and $m = 2$, we find

$$cD^+_{1_y} + \beta H^+_{1_x} = cD^+_{2_y} + \beta H^+_{2_x} + cD^-_{2_y} + \beta H^-_{2_x}, \tag{3.5a}$$

$$cB^+_{1_x} + \beta E^+_{1_x} = cB^+_{2_x} + \beta E^+_{2_x} + cB^-_{2_x} + \beta E^-_{2_x}. \tag{3.5b}$$

Defining the transmission and reflection coefficients as $T^+_{1,2} = A^{++}_2/A^+_1$, $\Gamma^+_{1,2} = A^{+-}_2/A^+_1$, as is shown in Fig. 3.2, and substituting (3.1) into (3.5) yields

$$n_1 - \beta\cos\theta^+_1 = \frac{\eta_1}{\eta_2}T^+_{1,2}\left(n_2 - \beta\cos\theta^+_2\right) + \Gamma^+_{1,2}\left(n_2 + \beta\cos\theta^-_2\right), \tag{3.6a}$$

$$n_1\cos\theta^+_1 - \beta = T^+_{1,2}\left(n_2\cos\theta^+_2 - \beta\right) - \Gamma^+_{1,2}\left(n_2\cos\theta^-_2 + \beta\right), \tag{3.6b}$$

with the definitions

$$Z^\pm_m = \eta_m g^\pm_m / f^\pm_m, \tag{3.7a}$$

$$g^\pm_m = n_m \mp \beta\cos\theta^\pm_m, \tag{3.7b}$$

$$f^\pm_m = n_m\cos\theta^\pm_m \mp \beta, \tag{3.7c}$$

with η_m being the intrinsic impedance of medium m. By replacing these into (3.6), we obtain

$$g^+_1 = \frac{\eta_1}{\eta_2}\left(g^+_2 T^+_{1,2} + g^-_2\Gamma^+_{1,2}\right), \tag{3.8a}$$

$$f^+_1 = \left(f^+_2 T^+_{1,2} - f^-_2\Gamma^+_{1,2}\right). \tag{3.8b}$$

Rearranging these equations yields the superluminal scattering coefficients at the interface between media $m = 1$ and $m = 2$ for a forward incident wave:

$$T^+_{1,2} = \frac{A^{++}_2}{A^+_1} = \frac{f^+_1}{f^+_2}\frac{\eta^2_2 Z^+_1 + \eta^2_1 Z^-_2}{\eta^2_1\left(Z^-_2 + Z^+_2\right)}, \tag{3.9a}$$

$$\Gamma^+_{1,2} = \frac{A^{+-}_2}{A^+_1} = \frac{f^+_1}{f^-_2}\frac{\eta^2_2 Z^+_1 - \eta^2_1 Z^+_2}{\eta^2_1\left(Z^-_{m+1} + Z^+_{m+1}\right)}. \tag{3.9b}$$

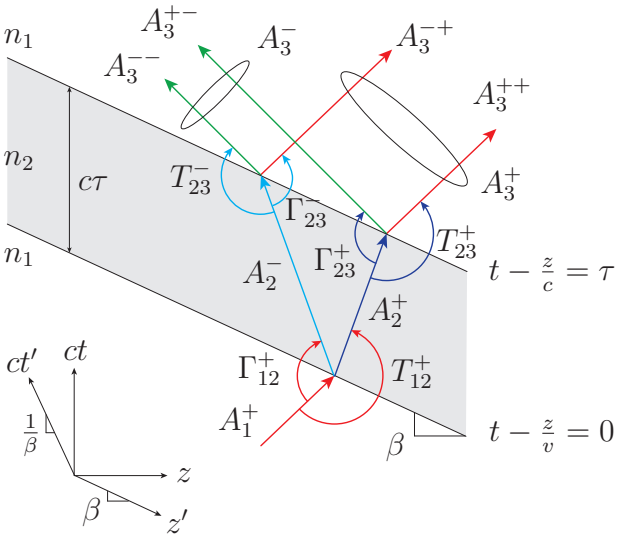

Figure 3.2 Scattering from a superluminal slab in the Minkowski diagram, leading to (3.9) and (3.14).

For normal incidence ($Z_i = \eta_i$ at normal incidence), (3.9) reduce to

$$T_{1,2}^{+} = \frac{(n_1 - \beta)}{(n_2 - \beta)} \frac{\eta_1 + \eta_2}{2\eta_1}, \tag{3.10a}$$

$$\Gamma_{1,2}^{+} = \frac{(n_1 - \beta)}{(n_2 + \beta)} \frac{\eta_1 - \eta_2}{2\eta_1}. \tag{3.10b}$$

These results correspond to those presented in Biancalana et al. (2007). From (3.10) we deduce the transmission and reflection coefficients from a temporal discontinuity ($\beta = 0$) are:

$$T_{12} = \frac{n_1}{n_2} \frac{\eta_2 + \eta_1}{2\eta_1}, \qquad \Gamma_{12} = \frac{n_1}{n_2} \frac{\eta_2 - \eta_1}{2\eta_1} \tag{3.11}$$

Which agrees with the result given by Morgenthaler (1958). The coefficients at the second interface are simply found by replacing n_1, n_2 by n_2, n_3.

$$T_{2,3}^{+} = \frac{A_3^{++}}{A_2^{+}} = \frac{f_2^{+}}{f_3^{+}} \frac{\eta_3^2 Z_1^{+} + \eta_2^2 Z_3^{-}}{\eta_2^2 \left(Z_3^{-} + Z_3^{+} \right)}, \tag{3.12a}$$

$$\Gamma_{2,3}^{+} = \frac{A_2^{+-}}{A_3^{+}} = \frac{f_2^{+}}{f_3^{-}} \frac{\eta_3^2 Z_2^{+} - \eta_2^2 Z_3^{+}}{\eta_2^2 \left(Z_3^{-} + Z_3^{+} \right)}, \tag{3.12b}$$

which reduce to, for normal incidence:

$$T^{+}_{2,3} = \frac{(n_2-\beta)}{(n_3-\beta)}\frac{\eta_2+\eta_3}{2\eta_2}, \tag{3.13a}$$

$$\Gamma^{+}_{2,3} = \frac{(n_2-\beta)}{(n_3+\beta)}\frac{\eta_3-\eta_2}{2\eta_2}. \tag{3.13b}$$

To find the coefficients of waves scattered by a backward incident wave, propagating in the $-z$ direction, we first notice that the problem of a backward wave exactly corresponds to that of a forward incident wave with the slab having the opposite direction: the scattering of a backward wave on a receding discontinuity is strictly equivalent to scattering of a forward wave on an approaching discontinuity. Thus, $T^{-}_{m,m+1} = T^{+}_{m,m+1}(-v_{\rm s})$, and $\Gamma^{-}_{m,m+1} = \Gamma^{+}_{m,m+1}(-v_{\rm s})$.

We are now equipped to solve the complete problem of scattering from a superluminal slab. Notice that whereas the subluminal STM slab supports an infinite number of waves scattered by the two interfaces, the superluminal slab scatters only two waves, a forward one and a backward one, at each interface, leading to a total of four scattered waves at the output of the system, as shown in Fig. 3.2. The corresponding overall scattering coefficients are obtained with the help of Fig. 3.2 by multiplying the successive scattering events and adding the final co-directed contributions, which yields

$$T = \frac{A^{+}_{3}}{A^{+}_{1}} = T^{+}_{12}T^{+}_{23}e^{-i\tau\omega^{+}_{2}} + \Gamma^{+}_{12}\Gamma^{-}_{23}e^{i\tau\omega^{-}_{2}}, \tag{3.14a}$$

$$\Gamma = \frac{A^{-}_{3}}{A^{+}_{1}} = T^{+}_{12}\Gamma^{+}_{23}e^{-i\tau\omega^{+}_{2}} + \Gamma^{+}_{12}T^{-}_{23}e^{i\tau\omega^{-}_{2}}, \tag{3.14b}$$

where the terms $e^{\mp i\tau\omega_2\pm}$ correspond to the phase accumulated across the slab. Figures 3.3(a),(b) plot the coefficients (3.14) as a function of the duration of the slab, τ, for velocity $v=-50c$ and $v=-5c$, for refractive indices $n_1=1$, $n_2=2$ and incident wave frequency $\omega_1 = 1$[rad/s], for the case of normal incidence ($\theta_1 = 0$). The coefficients are periodic, due to commensurability. For the lower velocity, the reflection and transmission coefficients are both greater than 1 at multiples of $\tau_{\max}$. This is not surprising, as this is a dynamic system, and therefore gain is expected. The transmission and reflection are synchronous: coefficients are maximal or minimal for the same values of τ. This is of course contrary to the case of spatial structures, where maximal transmission always corresponds to minimal transmission. All these concepts will be explained in greater detail in section 4.3.

We shall now derive the ST frequencies $(\mathbf{k}^{\pm}_{m}, \omega^{\pm}_{m})$ of a wave scattered from a superluminal slab. The quantities are first diagrammatically localized in the dispersion diagram in Fig. 3.4,

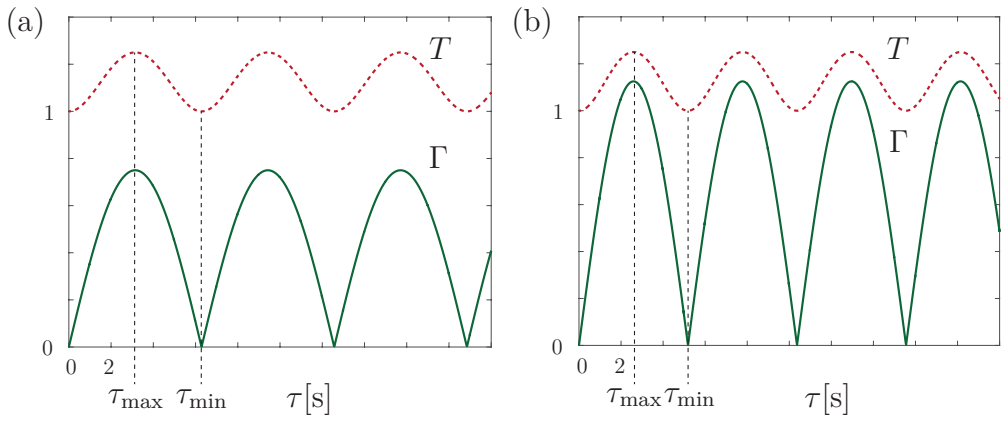

Figure 3.3 Scattering coefficients computed by (3.14), plotted as a function of τ[s]. (a) $v = -50c$. (b) $v = -5c$.

and will later be derived mathematically. The same method as in section 2.6.4 is applied. The superluminal discontinuity is solved in a frame moving at a speed such that the slab appears everywhere at once, i.e. appears as a temporal discontinuity. The spatial frequencies are found by applying the continuity condition of $\mathbf{k}'$ (see Fig. 2.11). The dispersion diagram this time is hyperbolic, since we are now considering an oblique wave (see Fig. 2.3). The diagram is constructed as follows: 1) Draw the frequency axes of both the static and moving frames. 2) Plot the dispersion curves of media $1 \equiv 3$ and 2 for a fixed k_x, corresponding to the incidence angle $\theta_1^+ = \sin^{-1}(k_{x1}^+/k_1^+)$. 3) Locate the incident field $\mathbf{E}_1^+$. 4) Trace the isofrequency lines parallel to the ω' axis (corresponding to conserved k_z'). 5) Locate the scattered field frequencies after the first discontinuity $\mathbf{E}_2^+$, $\mathbf{E}_2^-$. 6) Locate the scattered field frequencies after the second discontinuity $\mathbf{E}_3^+$, $\mathbf{E}_3^-$. The corresponding transitions in the direct space are shown in Fig. 3.2. Following these steps, we find that the transmitted field $\mathbf{E}_3^+$ has the same frequency than the incident field $\mathbf{E}_1^+$, whereas the reflected field $\mathbf{E}_3^+$ has been upshifted, but has a negative frequency.

We now proceed with the mathematical derivation. Wavenumber conservation in the moving frame, $\mathbf{k}_{\mathrm{i}}' = \mathbf{k}_{\mathrm{r,t}}'$, is expressed in the rest frame, using Lorentz transformation, as

$$k_{1z}^+ - \beta\frac{\omega_1^+}{c} = k_{2z}^\pm \mp \beta\frac{\omega_2^\pm}{c} = k_{3z}^\pm \mp \beta\frac{\omega_3^\pm}{c}, \tag{3.15a}$$

$$k_{1x}^+ = k_{2x}^\pm = k_{3x}^\pm. \tag{3.15b}$$

The scattered temporal frequencies are subsequently found by substituting $k_{mz}^\pm = k_m^\pm \cos\theta_m^\pm$ and $k_{mx}^\pm = k_m^\pm \sin\theta_m^\pm$ with $k_m^\pm = \omega_m^\pm n_m/c$ into (3.15a). These quantities were defined in

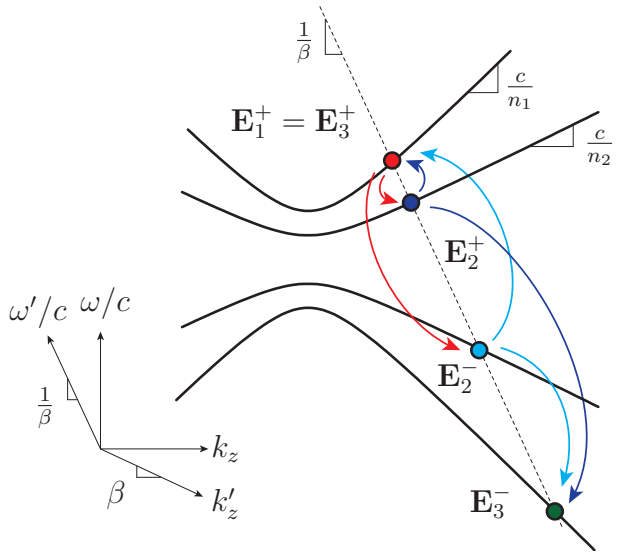

Figure 3.4 Transitions in the dispersion diagram, leading to (3.15) and (3.16).

Fig. 3.1. The results are

$$\omega_2^{\pm} = \omega_1^+ \frac{n_1 \cos\theta_1^+ - \beta}{n_2 \cos\theta_2^{\pm} \mp \beta} = \omega_1^+ \frac{f_1^+}{f_2^{\pm}}, \tag{3.16a}$$

$$\omega_3^+ = \omega_1^+ \frac{f_1^+}{f_3^+} = \omega_1^+, \quad \omega_3^- = \omega_1^+ \frac{f_1^+}{f_3^-} = \omega_1^+ \frac{n_1 \cos\theta_1^+ - \beta}{n_1 \cos\theta_3^- + \beta}. \tag{3.16b}$$

These equations reveal that the transmitted wave in the third medium has the same frequency as the incident wave, and that the backward wave depends on β, in accordance with the diagrammatic construction in Fig. 3.4. We next solve the angles of the scattered waves.

The scattering angles are obtained by substituting (3.1c) into (3.15b) and (3.15a), and dividing the resulting equations, which yields

$$\frac{\sin\theta_1^+}{\cos\theta_1^+ - \beta/n_1} = \frac{\sin\theta_2^{\pm}}{\cos\theta_2^{\pm} \mp \beta/n_2} = \frac{\sin\theta_3^{\pm}}{\cos\theta_3^{\pm} \mp \beta/n_1}. \tag{3.17}$$

Inspection of (3.17) and (3.16b) reveals that the transmitted wave has the same angle and frequency as the incident wave.

We next explicitly derive the angles of the scattered waves in the third medium, closely following the steps in Kunz (1980). Considering the initial and final media are free space, and so $k_m^{\pm} = \omega_m^{\pm}/c$, wavenumber conservation (3.15a) is written as

$$k_{z_1}^+ - \beta k_1^+ = k_{z_3}^- + \beta k_3^-, \tag{3.18}$$

which can be rearranged as

$$k_{z_1}^{+} - k_{z_3}^{-} = \beta \left(k_1^{+} + k_3^{-} \right). \tag{3.19}$$

Upon inserting the Helmholtz relation into the continuity condition of k_x (3.15b) and squaring, we obtain

$$k_1^{+\,2} - k_{z_1}^{+\,2} = k_3^{-\,2} - k_{z_3}^{-\,2}, \tag{3.20}$$

or, after rearranging,

$$k_{z_1}^{+\,2} - k_{z_3}^{-\,2} = k_1^{+\,2} - k_3^{-\,2}. \tag{3.21}$$

Equation (3.21) is rewritten as

$$(k_{z_1}^{+} - k_{z_3}^{-})(k_{z_1}^{+} + k_{z_3}^{-}) = (k_1^{+} - k_3^{-})(k_1^{+} + k_3^{-}), \tag{3.22}$$

and dividing (3.22) by (3.19) yields

$$k_{z_1}^{+} + k_{z_3}^{-} = \frac{1}{\beta} \left(k_1^{+} - k_3^{-} \right), \tag{3.23}$$

or

$$k_1^{+} - \beta k_{z_1}^{+} = k_3^{-} + \beta k_{z_3}^{-}. \tag{3.24}$$

Substituting $k_{zm}^{\pm} = k_m^{\pm} \cos\theta_m^{\pm}$ into (3.24) yields

$$k_1^{+}(1 - \beta \cos\theta_1^{+}) = k_3^{-} \left(1 + \beta \cos\theta_3^{-} \right), \tag{3.25}$$

while performing the same substitution into (3.18) gives

$$k_1^{+} \left(\cos\theta_1^{+} - \beta \right) = k_3^{-}(\cos\theta_3^{-} + \beta). \tag{3.26}$$

Finally, dividing (3.25) by (3.26) yields

$$\frac{1 - \beta \cos\theta_1^{+}}{\cos\theta_1^{+} - \beta} = \frac{1 + \beta \cos\theta_3^{-}}{\cos\theta_3^{-} + \beta}, \tag{3.27}$$

which rearranges to the closed-form solution

$$\cos\theta_3^{-} = \frac{\cos\theta_1^{+}\,(1 + \beta^2) - 2\beta}{1 + \beta^2 - 2\beta \cos\theta_1^{+}}. \tag{3.28}$$

3.2 Symmetries between Sup- and Super-luminal Slabs

We now uncover two fundamental symmetries between sub- and super-luminal slabs. One symmetry addresses the frequency and direction of propagation, and the other is related to the amplitude of the scattered waves.

First, let us point out a symmetry in the Minkowski diagram. In Fig. 3.5, we can see that spatial and temporal slabs, shown in Fig. 3.5(a), or more generally subluminal and superluminal slabs, in Fig. 3.5(b), are symmetric with respect to the light line if the width of the subluminal slab D is equal to the duration of the superluminal slab $c\tau$, and if the velocities are exactly opposite ($v_{\text{sub}}/c = c/v_{\text{sup}}$). This observation motivates our search for symmetries in the properties of the scattered waves.

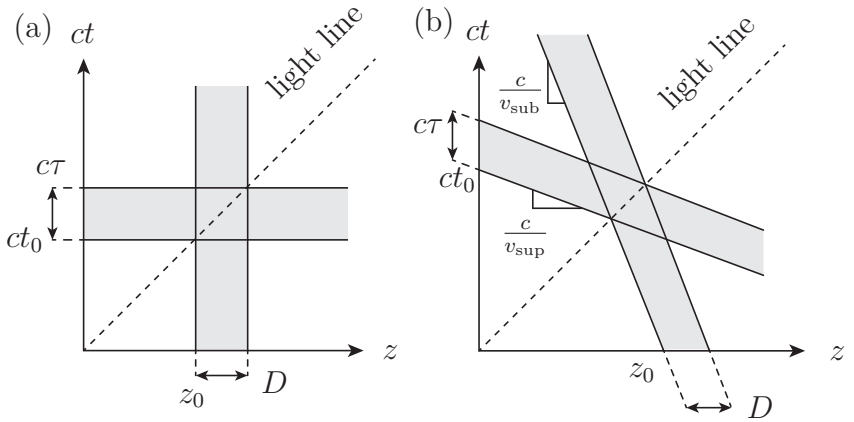

Figure 3.5 Symmetry of STM slabs. (a) Spatial and temporal slab. (b) Subluminal and superluminal STM (approaching) slab.

3.2.1 Symmetry ST Spectrum

Figure 3.6 illustrates the first symmetry, concerning the frequencies and the angles of the scattered waves. The top diagram is constructed as in Fig. 3.4, without the dispersion curve for the second medium, since we are interested only in the waves at the output of the slab.

The case of the *subluminal* slab is solved, remembering that the temporal frequencies in the moving frame (ω') are conserved, by drawing the dashed line parallel to the k'_z axis. For the *superluminal* slab, the spatial frequencies in the moving frame (k'_z) are conserved, and so we draw a the dashed line parallel to the ω' axis. The solutions for the subluminal and the superluminal slab are indicated, in red. The reflected field solutions are symmetric with respect to the dashed line corresponding to $\omega/c = k_z$. The temporal frequencies of the

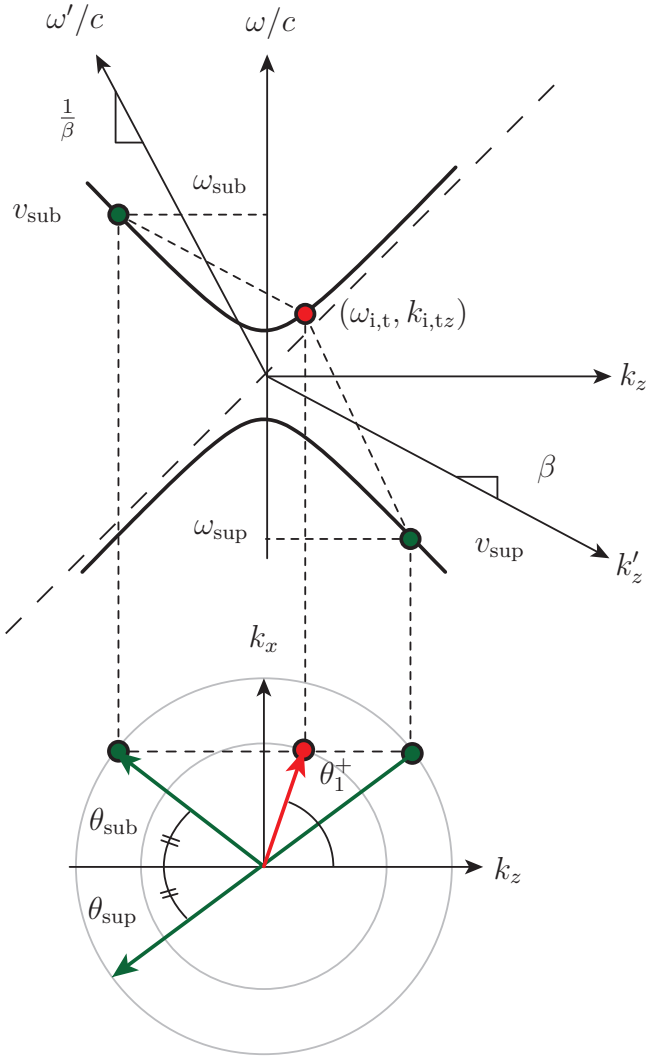

Figure 3.6 Demonstration of ST frequency symmetry between sub- and super-luminal slabs using dispersion and isofrequency diagrams.

reflected waves are equal in magnitude: $\omega_{\text{sub}} = -\omega_{\text{super}}$, and those of the transmitted wave are exactly equal: $\omega_{\text{i}} = \omega_{\text{t}}$.

The bottom diagram is the isofrequency diagram, and is constructed as follows: 1) Project the k_z value onto this (k_x, k_z) diagram. 2) Locate the intersection with the constant k_x line. 3) Draw the isofrequency circles with radii corresponding the intersection points. 4) Draw the normal to these isofrequency curves to find the corresponding group velocities ($\mathbf{v}_{\text{g}} = \nabla_{\mathbf{k}}\omega$).

We find that the subluminal slab is scattered at a smaller angle than the incidence angle. A possible intuitive interpretation would be to suggest that the slab has given momentum in the z direction to the wave.

The group velocity of the superluminal slab is drawn toward the center of the isofrequency, because the frequency is negative and so increasing the frequency corresponds to shrinking isofrequencies. It can be seen that the scattering angles of the superluminal and subluminal solutions are equal, but one points in the $+k_x$ and the other in the $-k_x$ direction.

This symmetry is also observed mathematically. We reproduce here the result of a wave reflected from a subluminal half-space, provided by Kunz (1980):

$$\cos\theta_3^- = \frac{\cos\theta_1^+\,(1+\beta^2) - 2\beta}{1+\beta^2 - 2\beta\cos\theta_1^+}. \tag{3.29}$$

and notice it is exactly the same as the one we derived, (3.28). However we recall that for subluminal problems, $\beta = v_{\text{m}}/c$, whereas for the superluminal problem, $\beta = c/v_{\text{m}}$. We express this symmetry as:

$$\theta_{3\ v_{\text{s}}>c}^-(v_{\text{s}}) = \theta_{3\ v_{\text{s}}<c}^-(1/v_{\text{s}}). \tag{3.30}$$

3.2.2 Symmetry Amplitude

The symmetry relating to the amplitude is studied for the particular case of normal incidence, where $\theta_1^+ = 0$ and therefore also $\theta_2^+ = \theta_2^- = 0$, according to (3.17). We show the derivation of the scattering coefficients for a subluminal slab in Appendix A.

We recall the superluminal slab equation (3.16a), which for normal incidence reduces to

$$\omega_2^+ = \omega_1^+\frac{n_1-\beta}{n_2-\beta}, \qquad \omega_2^- = \omega_1^+\frac{n_1-\beta}{n_2+\beta}. \tag{3.31}$$

Inserting the second equality of (3.16a) into (3.10) yields

$$T_{1,2}^+ = \frac{(n_1-\beta)}{(n_2-\beta)}\frac{n_1+n_2}{2n_2} = \frac{\omega_2^+}{\omega_1^+}\frac{n_1+n_2}{2n_2}, \tag{3.32a}$$

$$\Gamma^{+}_{1,2} = \frac{(n_1-\beta)}{(n_2+\beta)}\frac{n_1-n_2}{2n_2} = \frac{\omega_2^-}{\omega_1^+}\frac{n_1-n_2}{2n_2}, \tag{3.32b}$$

indicating that the scattering coefficients are proportional to the ratio of scattered versus incident frequencies. Equations (3.14) then yield $T \propto \omega_3^+/\omega_1^+ = 1$ and $\Gamma \propto \omega_3^-/\omega_1^+$, a result that also holds for subluminal STM slabs, as shown in (Pierce, 1958; Yeh and Casey, 1966). To observe this symmetry, we choose a subluminal slab of spatial extent $\zeta_{\text{sub}} = 5$ m and a superluminal slab of duration $c\tau_{\text{super}} = 5$ m, such that $\zeta_{\text{sub}} = c\tau_{\text{super}}$ as was suggested in Fig. 3.5. Figure 3.7 plots the amplitudes of the scattered waves versus β for a wave with frequency $\omega_1^+ = 1$ rad/s normally incident on a slab with index $n_2 = \sqrt{2}$ surrounded by media of indices $n_1 = n_3 = 1$. The grey areas of Fig. 3.7(a) correspond to regions without analytical solutions (Biancalana et al., 2007). Note that both solutions are functions of parameter β, but that β is proportional and inversely proportional to velocity for subluminal and superluminal slabs respectively. From Fig. 3.5, we deduce the symmetry

$$\text{envelope}\left\{\Gamma_{\text{sup}}(v_{\text{s}})\right\} \propto \text{envelope}\left\{\Gamma_{\text{sub}}(1/v_{\text{s}})\right\}, \tag{3.33a}$$

and the result

$$\min(T_{\text{sup}}) = \max(T_{\text{sub}}) = 1 \neq f(v_{\text{s}}). \tag{3.33b}$$

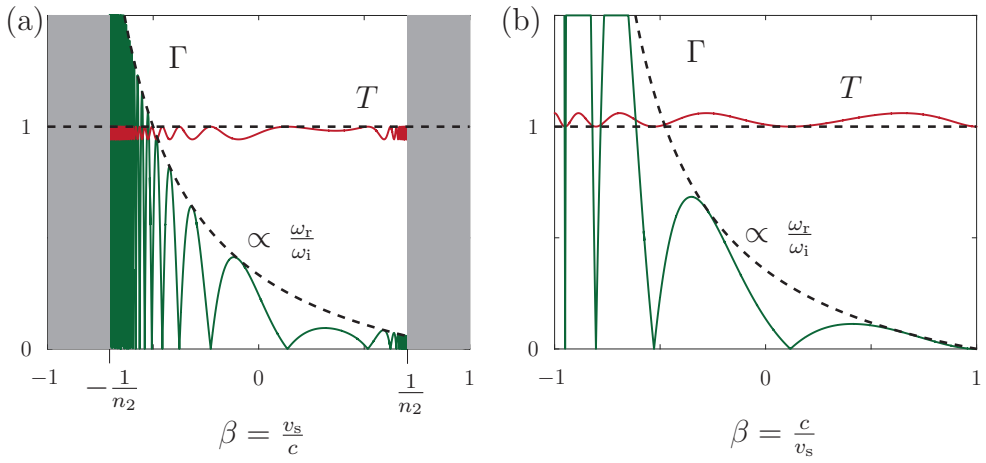

Figure 3.7 Scattering coefficients computed by (3.14). (a) Subluminal STM slab. (b) Superluminal STM slab.

3.3 Conclusion

The amplitudes and frequencies of waves scattered from a superluminal slab were calculated for an obliquely incident wave. It was found that the forward wave suffers no frequency shift and no change in direction, whereas the backward wave is both deflected and frequency shifted. The frequency shift was found to be the same as a wave reflected by a subluminal slab with opposite velocity. The deflection angles of the reflected wave were also shown to have a symmetric angle with respect to the subluminal case. The reflected wave is oriented towards the incident wave, which is impossible for subluminal slabs, and therefore new directions are attainable using superluminal slabs. This could lead to interesting applications, as the range of possible scattering angles is increased.

CHAPTER 4 SUPERLUMINAL STM CRYSTAL

4.1 Introduction

Stationary crystals are well known to exhibit band gaps at odd multiples of the spatial frequency modulation. These gaps are associated to a Bragg condition. In this section, we extend the Bragg condition to STM periodic structures, in particular to a superluminal crystal, which is a succession of superluminal slabs. An infinite superluminal crystal was solved by Cassedy (1967), who demonstrated that this structure gives rise to instabilities at the intersection of modes in a skewed dispersion diagram. We will deduce the position of these intersections by interferometric arguments, similar to the Bragg argument for stationary crystals. The following is an adaptation and an extension of (Deck-Léger and Caloz, 2017a)

4.1.1 Abrupt and Smooth Variations

A crystal made of abrupt discontinuities between media of refractive indices n_1, n_2 is represented in Fig. 4.1(a). This type of crystal has well-defined boundaries, and will be solved by applying periodic boundary conditions.

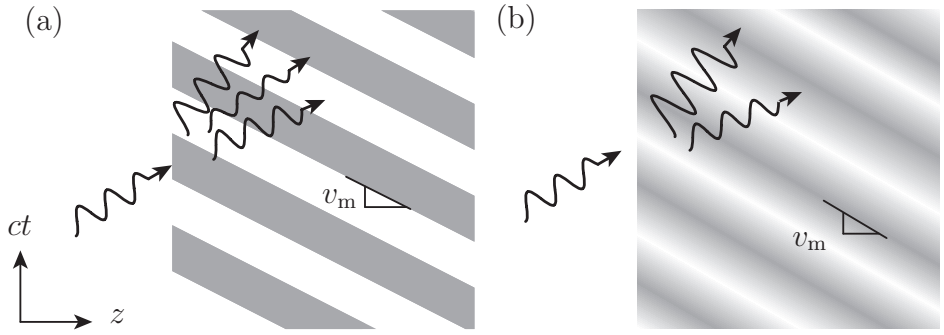

Figure 4.1 Superluminal crystals. (a) Based on abrupt discontinuities. (b) Based on smooth variations

A crystal made of smooth medium variations is represented in Fig. 4.1(b). This type of structure does *not* have clearly defined boundaries, and lends itself to a Bloch-Floquet treatment, as is done in Cassedy (1967). Indeed the Bloach-Floquet expansion is best suited for harmonic modulation or modulation that can be expanded into a finite number of harmonics. In the case of abrupt discontinuities, this approach is inconvenient. The crystal based on

abrupt discontinuities is modeled by an infinite number of harmonics, and so the computation would be slow. More importantly, the Gibbs phenomenon will appear, such that the discontinuities will not be perfectly modeled. Even by considering a very high number of harmonics, the result will be imprecise. We therefore see that the usual treatment using Bloch-Floquet expansion would not be suitable for the crystal with abrupt discontinuities we wish to study. Here, we suggest an alternative approach which circumvents this problem.

4.2 Introduction to Periodic STM Structures

We first introduce two crystals, a subluminal and a superluminal one, presented in Figs. 4.2(a), (c). Both have a periodic refractive index $n(z,t) = n(z+\zeta, t+\tau)$, where ζ and τ are the modulation wavelength and period, respectively, and therefore the modulation velocity is $v_{\rm m} = \zeta/\tau$. For inverse velocities $v_{\rm sub}/c = c/v_{\rm super}$, the two crystals are symmetric across the light line $z = ct$ if the the spatial period of the subluminal crystal is equal to the temporal period of the superluminal crystal, $\zeta_{\rm sub} = c\tau_{\rm sup}$. The corresponding dispersion diagrams are drawn in Figs. 4.2(b), (d) for an infinitesimally small modulation. The temporal and spatial modulation frequencies are $\Omega = 2\pi/\tau$ and $K = 2\pi/\zeta$, respectively. These diagrams are also symmetric by reflection across the $\omega = kc$ line. Here, we explain how to construct these dispersion diagrams.

The subluminal dispersion diagram is constructed by first drawing the frequency axes for the stationary and the moving frames. Since the crystal appears to be stationary in the moving frame, the periodicity of the modes is along the k'_z axis. The origins of the modes are located at points mK, $m\Omega$, with $m = 1, 2, 3....$ From these points, the complete diagram can be drawn for infinitesimal modulation, with harmonic slopes $n_{\rm av}$. For stronger modulation, gaps open up, corresponding to attenuation regions.

To construct the superluminal dispersion diagram, we first draw the frequency axes for the stationary and the moving frames. Since the crystal appears as purely temporal in the moving frame, the crossing points of the harmonics are located on the ω'/c axis. From the knowledge of the spatial and temporal frequencies K, Ω, the origins of the modes are located. From these points, the complete diagram can be drawn for infinitesimal modulation, with harmonic slopes $n_{\rm av}$. For stronger modulation, gaps open up, corresponding to unstable (amplification) regions, as will be shown. Notice the dispersion diagrams are symmetric with respect to the free space $\omega/c = k_z$ line.

Figure 4.3 presents an FDTD simulation of a 3 period superluminal crystal with $v_{\rm p} = -3c$ illuminated by a modulated Gaussian pulse. The color represents the amplitude of the waves.

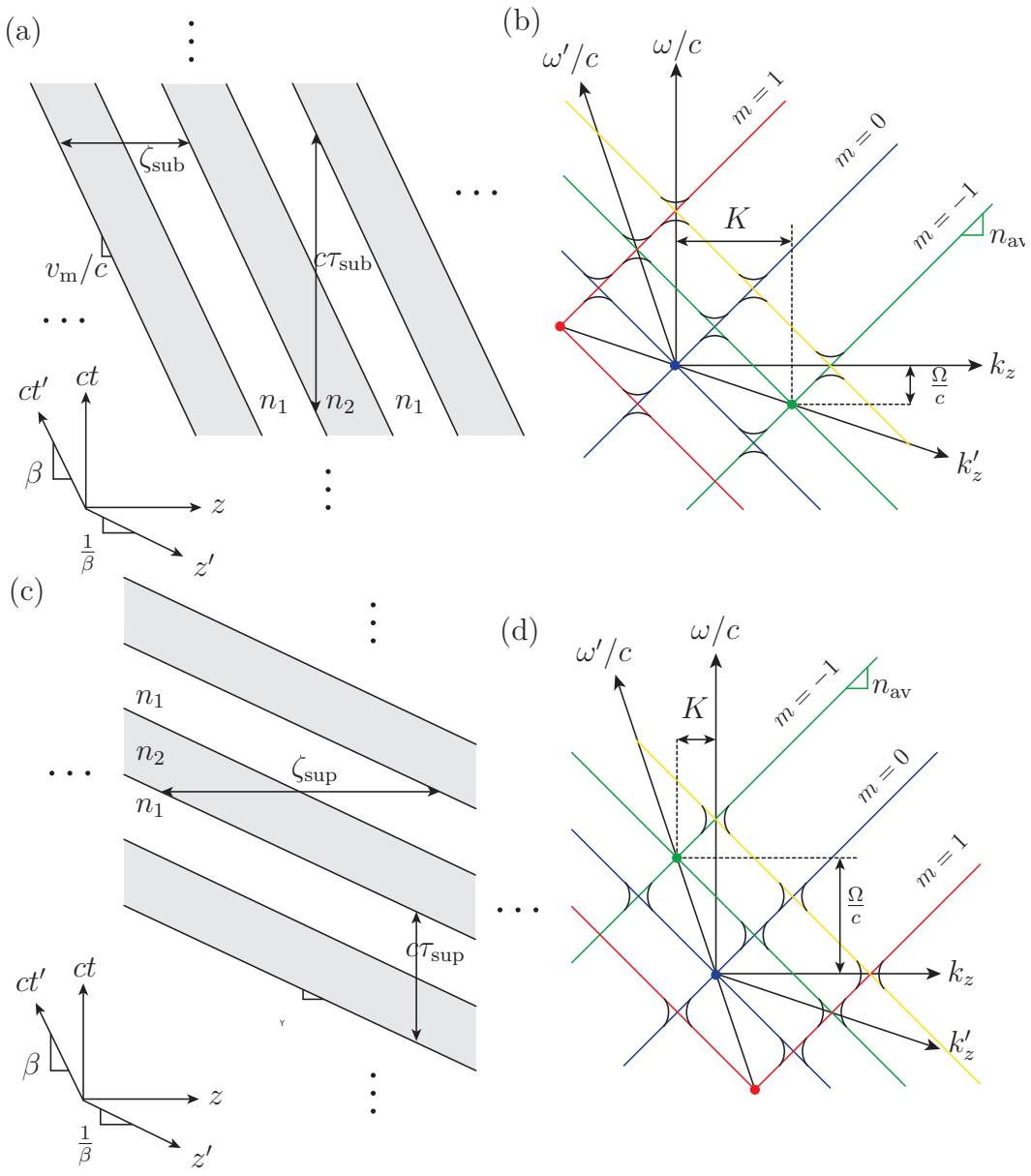

Figure 4.2 STM Crystals. (a) Subluminal, Minkowski representation. (b) Subluminal, dispersion diagram. (c) Superluminal, Minkowski representation. (b) Superluminal, dispersion diagram.

The refractive index profile is projected on the space and time axes. The refractive indices of the background and slab media are $n_1 = 1$ and $n_2 = 2$, respectively. The durations are $\tau_1 = \tau_2 = \tau/2 = 4T_1$, corresponding to the distances $\zeta_1 = \zeta_2 = \zeta/2 = 4|v_{\text{p}}|T_1$, with T_1 the period of the incident wave. The output waves have been amplified, suggesting that an infinite crystal would be unstable.

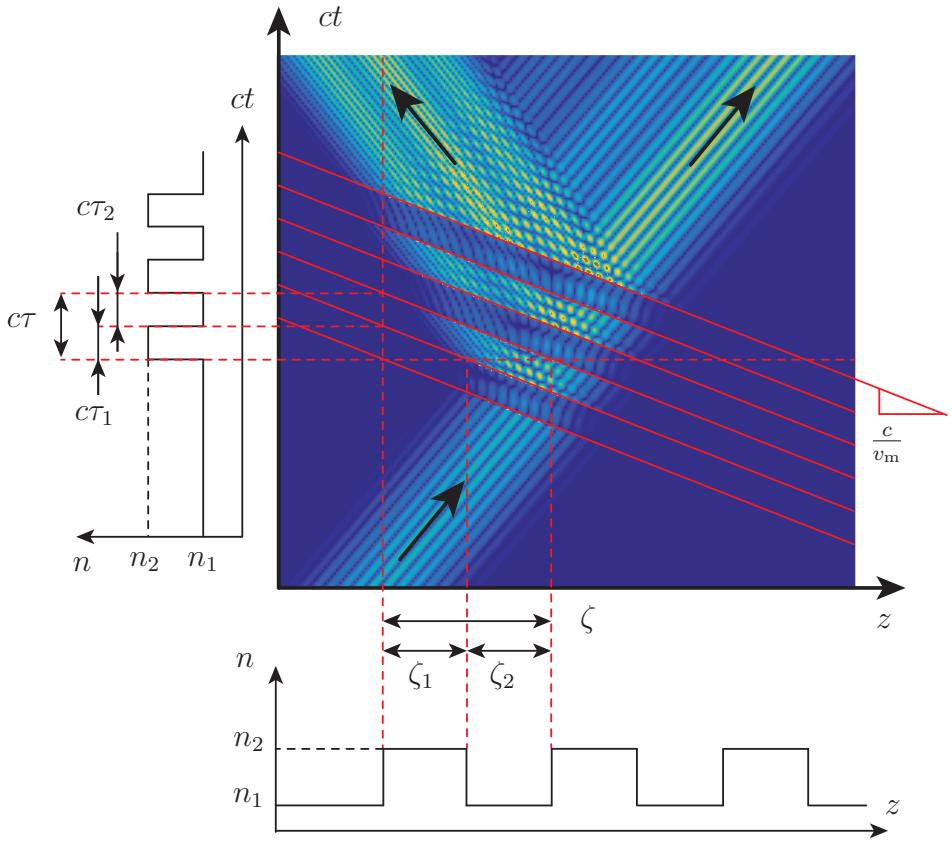

Figure 4.3 FDTD-simulated scattering of a modulated Gaussian pulse on a three-period approaching superluminal crystal.

4.2.1 Matrix Formulation

We now want to solve a succession of superluminal slabs. We will use a matrix formulation, adapted from the matrix formulation of stationary scattering problems (Collins, 1991). The fields are defined in Fig. 4.4, where $E_{m,n}$ is defined as the field in medium m at interface n. The $+, -$ superscripts refer to the propagation direction, as usual. The fields scattered from the first interface are related to the incident forward and backward fields as:

$$\begin{bmatrix} E^+_{2,1} \\ E^-_{2,1} \end{bmatrix} = \begin{bmatrix} T^+_{12} & \Gamma^-_{12} \\ \Gamma^+_{12} & T^-_{12} \end{bmatrix} \begin{bmatrix} E^+_{1,1} \\ E^-_{1,1} \end{bmatrix}, \tag{4.1}$$

where the coefficients were calculated in (3.9). The propagation matrix relates the fields

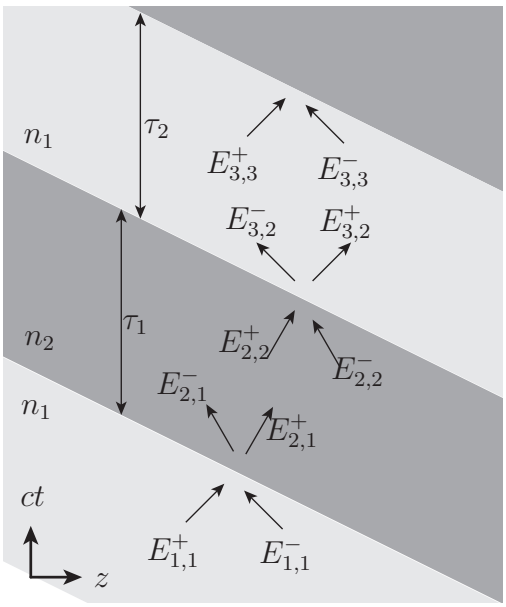

Figure 4.4 Definition of fields for superluminal slab calculations

inside the slab from the first interface to the second interface:

$$\begin{bmatrix} E^+_{2,2} \\ E^-_{2,2} \end{bmatrix} = \begin{bmatrix} e^{i\phi^+_1} & 0 \\ 0 & e^{i\phi^-_1} \end{bmatrix} \begin{bmatrix} E^+_{2,1} \\ E^-_{2,1} \end{bmatrix}. \tag{4.2}$$

where the phase $\phi^\pm_1 = \omega^\pm_2 \tau_1$. The matching matrix at the second interface is:

$$\begin{bmatrix} E^+_{3,2} \\ E^-_{3,2} \end{bmatrix} = \begin{bmatrix} T^+_{23} & \Gamma^-_{23} \\ \Gamma^+_{23} & T^-_{23} \end{bmatrix} \begin{bmatrix} E^+_{2,2} \\ E^-_{2,2} \end{bmatrix} \tag{4.3}$$

and the final propagation matrix is:

$$\begin{bmatrix} E^+_{3,3} \\ E^-_{3,3} \end{bmatrix} = \begin{bmatrix} e^{i\phi^+_2} & 0 \\ 0 & e^{i\phi^-_2} \end{bmatrix} \begin{bmatrix} E^+_{3,2} \\ E^-_{3,2} \end{bmatrix}, \tag{4.4}$$

with the phase $\phi^\pm_2 = \omega^\pm_1 \tau_2$. Finally, cascading the matrices yields

$$\begin{bmatrix} E^+_{3,3} \\ E^-_{3,3} \end{bmatrix} = \begin{bmatrix} e^{i\phi^+_2} & 0 \\ 0 & e^{i\phi^-_2} \end{bmatrix} \begin{bmatrix} T^+_{23} & \Gamma^-_{23} \\ \Gamma^+_{23} & T^-_{23} \end{bmatrix} \begin{bmatrix} e^{i\phi^+_1} & 0 \\ 0 & e^{i\phi^-_1} \end{bmatrix} \begin{bmatrix} T^+_{12} & \Gamma^-_{12} \\ \Gamma^+_{12} & T^-_{12} \end{bmatrix} \begin{bmatrix} E^+_{1,1} \\ E^-_{1,1} \end{bmatrix}, \tag{4.5}$$

we then multiply the matrices to obtain

$$\begin{bmatrix} E^+_{3,3} \\ E^-_{3,3} \end{bmatrix} = \begin{bmatrix} e^{i\phi_2^+}\left(T^+_{23}T^+_{12}e^{i\phi_1^+} + \Gamma^-_{23}\Gamma^+_{12}e^{i\phi_1^-}\right) & e^{i\phi_2^+}\left(T^+_{23}\Gamma^-_{12}e^{i\phi_1^+} + \Gamma^-_{23}T^-_{12}e^{i\phi_1^-}\right) \\ e^{i\phi_2^-}\left(\Gamma^+_{23}T^+_{12}e^{i\phi_1^+} + T^-_{23}\Gamma^+_{12}e^{i\phi_1^-}\right) & e^{i\phi_2^-}\left(\Gamma^+_{23}\Gamma^-_{12}e^{i\phi_1^+} + T^-_{23}T^-_{12}e^{i\phi_1^-}\right) \end{bmatrix} \begin{bmatrix} E^+_{1,1} \\ E^-_{1,1} \end{bmatrix}. \quad (4.6)$$

The fields are relabelled such that $E^+_{n,n} = E_{m=(n-1)/2}$, corresponding to the field at the m'th period,

$$\begin{bmatrix} E^+_{m+1} \\ E^-_{m+1} \end{bmatrix} = [T] \begin{bmatrix} E^+_m \\ E^-_m \end{bmatrix}. \quad (4.7)$$

To solve the propagation problem of m slabs, we can simply cascade the matrix $[T]$, such that:

$$\begin{bmatrix} E^+_m \\ E^-_m \end{bmatrix} = [T]^{m-1} \begin{bmatrix} E^+_1 \\ E^-_1 \end{bmatrix}. \quad (4.8)$$

4.3 Intereference Analysis of Single Slab

Before computing (4.8), we reexamine a superluminal slab, seeking the conditions for maximal and minimal interference. The transmitted and reflected field coefficients for a single interface were found in section 3.1, equation (3.9) as

$$T^+_{m,m+1} = \frac{A^{++}_{m+1}}{A^+_m} = \frac{f^+_m}{f^+_{m+1}} \frac{\eta^2_{m+1}Z^+_m + \eta^2_m Z^-_{m+1}}{\eta^2_m\left(Z^-_{m+1} + Z^+_{m+1}\right)}, \quad (4.9a)$$

$$\Gamma^+_{m,m+1} = \frac{A^{+-}_{m+1}}{A^+_m} = \frac{f^+_m}{f^-_{m+1}} \frac{\eta^2_{m+1}Z^+_m - \eta^2_m Z^+_{m+1}}{\eta^2_m\left(Z^-_{m+1} + Z^+_{m+1}\right)}. \quad (4.9b)$$

For normal incidence from medium 1 to medium 2, substituting $f^+_1/f^\pm_2 = \omega^+_1/\omega^\pm_2$, (equation (3.16)) these reduce to:

$$T^+_{12} = \frac{f^+_1}{f^+_2}\frac{(\eta_2+\eta_1)}{2\eta_1} = \frac{\omega^+_1 n_2}{\omega^+_2 n_1}T^\infty_{12}, \quad T^-_{12} = \frac{\omega^-_1 n_2}{\omega^-_2 n_1}T^\infty_{12}, \quad (4.10a)$$

$$\Gamma^+_{12} = \frac{f^+_1}{f^-_2}\frac{(\eta_2-\eta_1)}{2\eta_1} = \frac{\omega^+_1 n_2}{\omega^-_2 n_1}\Gamma^\infty_{12}, \quad \Gamma^-_{12} = \frac{\omega^-_1 n_2}{\omega^+_2 n_1}\Gamma^\infty_{12}, \quad (4.10b)$$

where $T^\infty_{12} = (n_1/n_2)(\eta_2+\eta_1)/2\eta_1$ and $\Gamma^\infty_{12} = (n_1/n_2)(\eta_2-\eta_1)/2\eta_1$ are the forward and backward coefficients from a temporal discontinuity from medium 1 to medium 2 (equation (3.11)). Similarly the coefficients from medium 2 to medium 3 reduce to

$$T^+_{23} = \frac{\omega^+_2 n_1}{\omega^+_3 n_2}T^\infty_{23}, \qquad T^-_{23} = \frac{\omega^-_2 n_1}{\omega^-_3 n_2}T^\infty_{23}, \quad (4.11a)$$

$$\Gamma_{23}^{+} = \frac{\omega_2^{+} n_1}{\omega_3^{-} n_2} \Gamma_{23}^{\infty}, \qquad \Gamma_{23}^{-} = \frac{\omega_2^{-} n_1}{\omega_3^{+} n_2} \Gamma_{23}^{\infty}. \tag{4.11b}$$

The total scattering coefficients from a slab were found as (3.14)

$$T = \frac{A_3^{+}}{A_1^{+}} = T_{12}^{+} T_{23}^{+} e^{-i\tau\omega_2^{+}} + \Gamma_{12}^{+} \Gamma_{23}^{-} e^{i\tau\omega_2^{-}}, \tag{4.12a}$$

$$\Gamma = \frac{A_3^{-}}{A_1^{+}} = T_{12}^{+} \Gamma_{23}^{+} e^{-i\tau\omega_2^{+}} + \Gamma_{12}^{+} T_{23}^{-} e^{i\tau\omega_2^{-}}. \tag{4.12b}$$

Inserting (4.10) and (4.11) into (4.12) yields

$$T = \frac{\omega_3^{+}}{\omega_1^{+}} \left(T_{12}^{\infty} T_{23}^{\infty} e^{-i\tau\omega_2^{+}} + \Gamma_{12}^{\infty} \Gamma_{23}^{\infty} e^{i\tau\omega_2^{-}} \right) = \left(T_{12}^{\infty} T_{23}^{\infty} e^{-i\tau\omega_2^{+}} + \Gamma_{12}^{\infty} \Gamma_{23}^{\infty} e^{i\tau\omega_2^{-}} \right), \tag{4.13a}$$

$$\Gamma = \frac{\omega_3^{-}}{\omega_1^{+}} \left(T_{12}^{\infty} \Gamma_{23}^{\infty} e^{-i\tau\omega_2^{+}} + \Gamma_{12}^{\infty} T_{23}^{\infty} e^{i\tau\omega_2^{-}} \right). \tag{4.13b}$$

The first and second terms of the reflection and transmission coefficients (4.13) are

$$T_{12}^{\infty} T_{23}^{\infty} = \left(\frac{\eta_1 + \eta_2}{2\eta_1} \right) \left(\frac{\eta_1 + \eta_2}{2\eta_2} \right) = \frac{\eta_1^2 + 2\eta_1\eta_1 + \eta_2^2}{4\eta_1\eta_2}, \tag{4.14a}$$

$$\Gamma_{12}^{\infty} \Gamma_{23}^{\infty} = - \left(\frac{\eta_1 - \eta_2}{2\eta_1} \right) \left(\frac{\eta_1 - \eta_2}{2\eta_2} \right) = - \frac{\eta_1^2 - 2\eta_1\eta_1 + \eta_2^2}{4\eta_1\eta_2}, \tag{4.14b}$$

$$T_{12}^{\infty} \Gamma_{23}^{\infty} = - \left(\frac{\eta_1 + \eta_2}{2\eta_1} \right) \left(\frac{\eta_1 - \eta_2}{2\eta_2} \right) = - \left(\frac{\eta_1^2 - \eta_2^2}{4\eta_1\eta_2} \right), \tag{4.14c}$$

$$\Gamma_{12}^{\infty} T_{23}^{\infty} = \left(\frac{\eta_1 - \eta_2}{2\eta_1} \right) \left(\frac{\eta_1 + \eta_2}{2\eta_2} \right) = \frac{\eta_1^2 - \eta_2^2}{4\eta_1\eta_2}. \tag{4.14d}$$

Inserting (4.14) into (4.13) yields the total transmission and reflection coefficients

$$T = \frac{1}{4\eta_1\eta_2} \left[\left(\eta_1^2 + \eta_2^2 \right) \left(e^{-i\tau\omega_2^{+}} - e^{i\tau\omega_2^{-}} \right) + 2\eta_1\eta_1 \left(e^{-i\tau\omega_2^{+}} + e^{i\tau\omega_2^{-}} \right) \right], \tag{4.15a}$$

$$\Gamma = - \frac{\omega_3^{-}}{\omega_1^{+}} \left(\frac{\eta_1^2 - \eta_2^2}{4\eta_1\eta_2} \right) \left(e^{-i\tau\omega_2^{+}} - e^{i\tau\omega_2^{-}} \right). \tag{4.15b}$$

Analysing (4.15), we find the the conditions for maximal or minimal amplitudes are

$$e^{-i\tau_{\max}\omega_2^{+}} + e^{i\tau_{\max}\omega_2^{-}} = 0 \quad (\text{and} \quad e^{-i\tau_{\max}\omega_2^{+}} - e^{i\tau_{\max}\omega_2^{-}} = 2), \tag{4.16a}$$

$$e^{-i\tau_{\min}\omega_2^{+}} - e^{i\tau_{\min}\omega_2^{-}} = 0 \quad (\text{and} \quad e^{-i\tau_{\min}\omega_2^{+}} + e^{i\tau_{\min}\omega_2^{-}} = 2), \tag{4.16b}$$

where the condition to the right in parenthesis is equivalent to the condition to the left. The corresponding extremum values are:

$$T_{\max} = \frac{\eta_1^2 + \eta_2^2}{4\eta_1\eta_2}, \qquad T_{\min} = 1, \tag{4.17a}$$

$$|\Gamma|_{\max} = \frac{\omega_3^-}{\omega_1^+}\left(\frac{\eta_1^2 - \eta_2^2}{4\eta_1\eta_2}\right), \qquad |\Gamma|_{\min} = 0. \tag{4.17b}$$

Equation (4.16) may be rewritten as

$$e^{i\tau_{\min}(\omega_2^- + \omega_2^+)} = 1, \quad e^{i\tau_{\max}(\omega_2^- + \omega_2^+)} = -1. \tag{4.18}$$

Which yields

$$\tau_{\min}(\omega_2^- + \omega_2^+) = 2q\pi, \quad \tau_{\max}(\omega_2^- + \omega_2^+) = (2q-1)\pi. \tag{4.19}$$

With $q = 1, 2, 3, ...$ an integer. From this, we conclude that $\tau_{\max} = (2q-1)/2\tau_{\min}$, which is consistent with Fig. 4.6(a). Recalling (3.16a), and reducing to the case of normal incidence,

$$\omega_2^{\pm} = \omega_1^+ \frac{n_1 \cos\theta_1^+ - \beta}{n_2 \cos\theta_2^{\pm} \mp \beta} = \omega_1^+ \frac{n_1 - \beta}{n_2 \mp \beta}, \tag{4.20}$$

and substituting this into (4.19) gives:

$$\frac{\tau_{\min}}{T_1^+} = q\frac{(n_2+\beta)(n_2-\beta)}{2n_2(n_1-\beta)}, \tag{4.21a}$$

$$\frac{\tau_{\max}}{T_1^+} = (2q-1)\frac{(n_2+\beta)(n_2-\beta)}{4n_2(n_1-\beta)} \tag{4.21b}$$

These results were verified by superposing the interference conditions to the plot of the reflection coefficient (4.12b) for $v_{\sup} = -3c$, with $\omega_1^+ = 1$. The reflection coefficient is plotted as a function of the refractive index contrast, n_2/n_1, and the duration of the slab normalized to the incident wave period, τ/T_1^+. The white lines are the interference condition for minimal amplification (4.21a), corresponding to $q = 1, 2, 3, 4$.

These interference conditions can be understood by the help of Fig. 4.6(b), which shows the condition for constructive interference in the Minkwoski diagram for duration $\tau_{\max}$. The full lines correspond to the trajectory of the maxima, whereas the dashed trajectories correspond to minima. The reflection coefficient after the first interface, going from medium n_1 to n_2, is negative for $\eta_1 > \eta_2$:

$$\Gamma_{12}^+ = \frac{\omega_1^+}{\omega_2^-}\frac{\eta_2 - \eta_1}{2\eta_1} < 1, \tag{4.22}$$

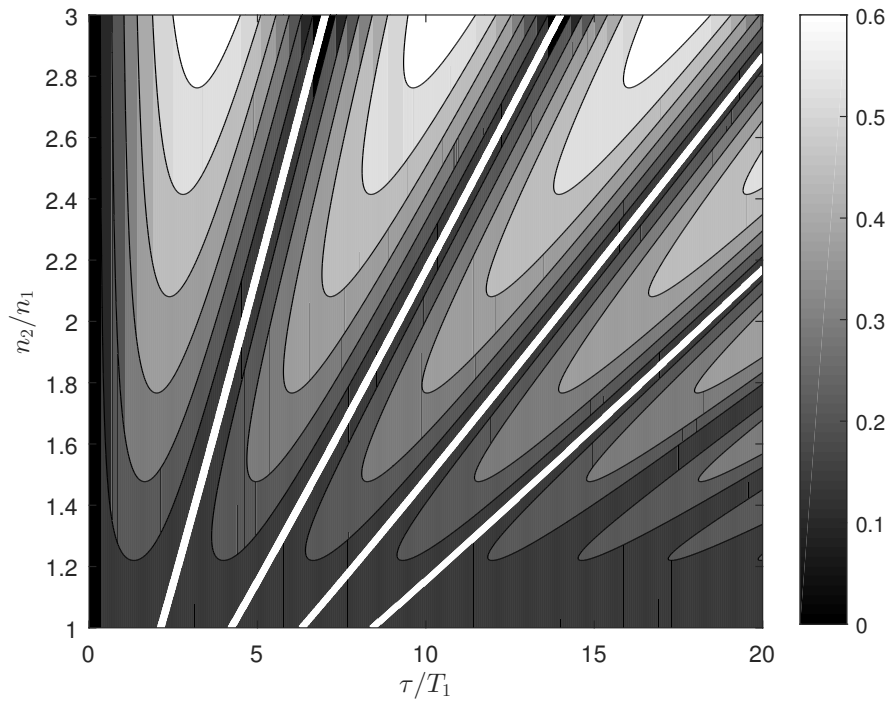

Figure 4.5 Plot of reflection coefficient (4.12b) from superluminal slab, with destructive interference corresponding to (4.21a) superimposed in white.

and therefore the full line transforms to a dashed line after the first interface. The reflection coefficient is positive going from medium n_2 to n_1:

$$\Gamma_{23}^{+} = \frac{\omega_2^{+}}{\omega_3^{-}} \frac{\eta_1 - \eta_2}{2\eta_1} > 1. \tag{4.23}$$

and so the full (dashed) lines remain full (dashed) lines at the second interface. There is constructive interference between the waves exiting the second medium. Normally there would be four scattered waves, but when the waves emerge in phase, there are only two scattered waves. This is the condition for maximal amplification.

4.3.1 Superluminal STM Crystal Instability Conditions

We now extend the previous results to the case of a succession of slabs. This is verified by cascading the matrices (4.8), as described in section 4.2.1. The amplitudes of the scattered waves after each period of the crystal are plotted in Fig. 4.7, for a slab moving at velocity $v_{\mathrm{m}} = -3c$ of refractive index $n_2 = 2$ surrounded by refractive index n_1 and duration τ satisfying (4.21a). The dashed lines correspond to the scattering of a forward incident wave

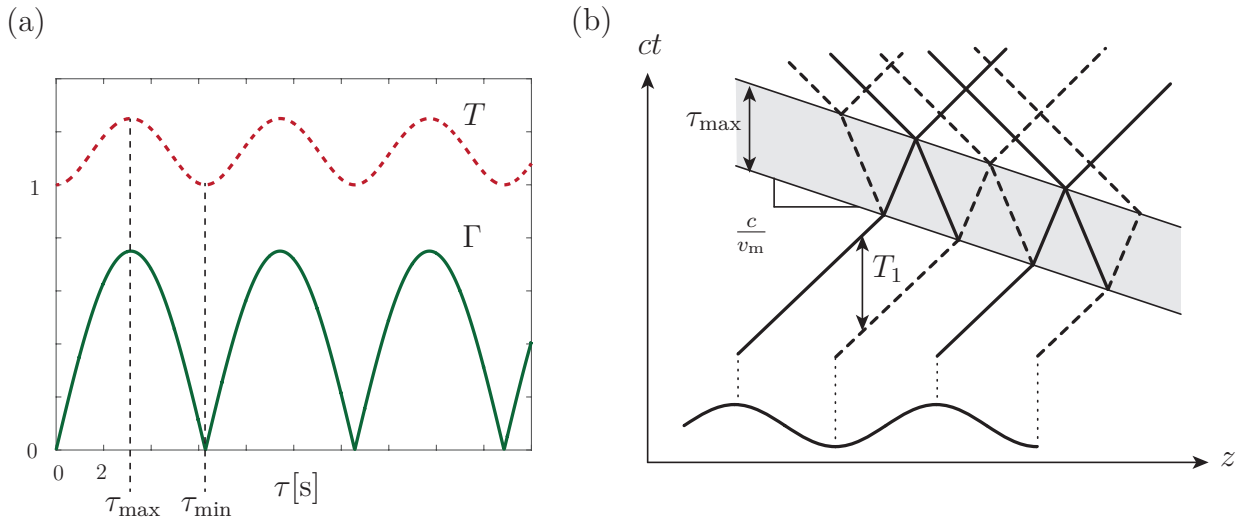

Figure 4.6 Interference illustrations corresponding to (4.21). (a) Scattering coefficients. (a) Constructive interference. (b) Destructive interference, for $\tau_{\min} = 2\tau_{\max}$.

with amplitude $A_1^+ = 1$ and frequency $\omega_1^+ = 1$. The red lines correspond to scattering from forward and backward incident waves $A_1^+ = 1$, $A_1^- = 0.5$ and $\omega_1^\pm = 1$. We see for the first case the amplitudes are constant, there is neither amplification nor decay, and for the second case the backward wave is evanescent and the forward wave stabilises after a few oscillations to $T = 1.2$. + Fig. 4.7(b) plots the amplitudes of the same specifications as before, but with the period of the crystal τ satisfying (4.21b).

We know want to connect these observations with the location of insability gaps in the dispersion diagram. In order to express the interference conditions in the frequency domain, we substitute $\tau_{\max} = \pi/\Omega$, $T_1^+ = 2\pi/\omega_1^+$ into (4.21b). Considering $n_1 = n_2 = n_{\text{av}}$ yields the condition for constructive interference in the frequency domain

$$\omega_{\min} = 2q\frac{(n_{\text{av}} + \beta)}{2n_{\text{av}}}\Omega, \tag{4.24a}$$

$$\omega_{\max} = (2q - 1)\frac{(n_{\text{av}} + \beta)}{2n_{\text{av}}}\Omega. \tag{4.24b}$$

Figure 4.8 presents the dispersion diagram of a superluminal crystal of velocity $v = -3c$. From (4.24), remembering that $\beta = c/v = 1/3$, we find $q = 1 \rightarrow \omega_1^+ = 2\Omega/3$ and $q = 0 \rightarrow \omega_1^+ = -2\Omega/3$. These solutions are boxed in green in Fig. 4.8. From these solutions, all the other instability regions can be found by translating by the vector Ω, K, drawn in blue arrows.

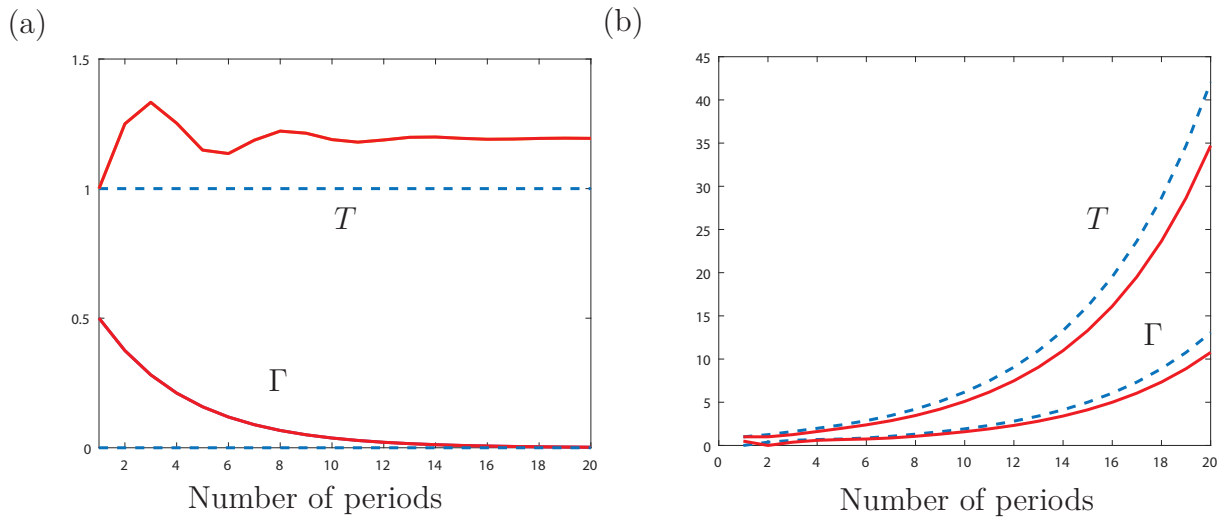

Figure 4.7 Scattering coefficients as a function of the number of periods of a superluminal crystal, satisfying (a) the destructive interference condition (4.21a), (b) the constructive interference condition (4.21b).

Figure 4.9 presents an FDTD simulation of a 16 period superluminal crystal with $v_\mathrm{p} = -3c$ illuminated by a modulated Gaussian pulse. The refractive indices of the background and slab media are $n_1 = 1$ and $n_2 = 1.5$, respectively. Figure 4.9(a) represents the results in the Minkowski diagram. The temporal modulation period is $\tau = T_1$, with the corresponding spatial modulation period $\zeta = |v_\mathrm{p}|T_1$, with T_1 the period of the incident wave. Figure 4.9(b) represents the two-dimensional numerical Fourier transform of Fig. 4.9(a), computed using the waves inside the crystal only. We clearly see a periodic pattern of amplification, with spatial frequency $K/k_{z0} = 1$ and temporal frequency $\Omega/\omega_0 = 1/3$, aligned on a slope of v_m/c corresponding to the slope of the ω'/c axis of Fig.4.8. Notice that there is no amplification along the central diagonal, corresponding to the ω'/c axis. Our method does not predict this, and we are currently looking for an explanation.

4.4 Conclusion

This chapter derived the amplification regions of a superluminal crystal. The results were derived by studying the interference conditions. Although the dispersion diagram of a superluminal crystal had already been derived in other papers, the analysis here gives further insight into the problem. Using the matrix approach we suggest, it is simple to study the amplitude of scattered waves after a finite number of slabs. This tool is useful for the analysis of sharp discontinuity superluminal crystals.

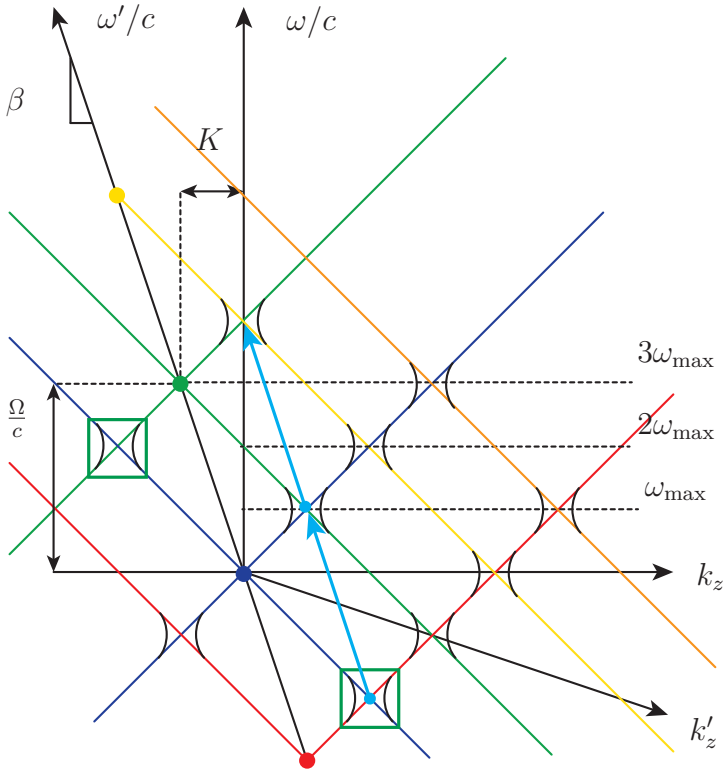

Figure 4.8 Position of superluminal STM crystal instabilities in the dispersion diagram given in (4.24)

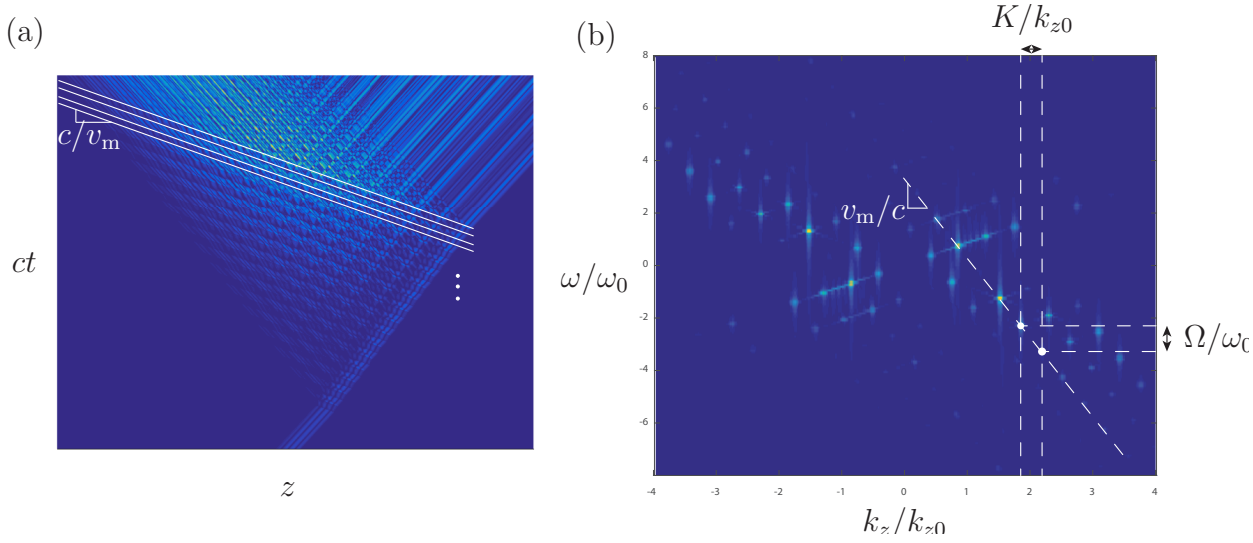

Figure 4.9 FDTD-simulated scattering of a modulated Gaussian pulse on a 16-period approaching superluminal crystal. (a) Direct space. (b) Inverse space.

CHAPTER 5 OTHER STM PERIODIC STRUCTURES

In this chapter, we present two applications of periodic STM structures. The first application is the focusing a pulse following reflection, realized by exploiting the curvature of the dispersion diagram of a dispersive structure and the nonreciprocity of subluminal crystals. This work is related to works on pulse compression by dispersion compensation.

The second application is an explanation of the inverse Doppler effect that occurs in periodic structures. The explanation of the inverse Doppler effect in periodic structures has stirred some controversy (Seddon and Bearpark, 2004; Reed et al., 2004; Kozyrev and van der Weide, 2005, 2006), but we do not address it directly. The explanation provided here is based on the diagrammatic method provided in chapter 2, and matches the theoretical predictions.

5.1 Focusing in Subluminal STM crystal

Here we show the focusing of waves after reflection in a subluminal crystal, adapted from (Deck-Léger and Caloz, 2017b). We first recall the principle of dispersion compensation in transmission, show how it can be done in reflection, and finally suggest an STM periodic structure that may achieve the desired ST focusing.

5.1.1 Focusing in Transmission

Focusing, or compression, is conventionally realized using dispersion compensation. This has some applications in wireless communication, where a signal is dispersed before being sent, and then is recompressed after reception (Abielmona et al., 2009). Figure 5.1 illustrates the principle. Figure 5.1(a) shows the trajectory of a pulse that suffers dispersion in one medium, and is then recompressed in the second medium. The corresponding spectrum is plotted in Fig. 5.1(b). The incident pulse ψ_i is launched at $(z,t)=(0,0)$, and propagates to the right in medium 1 ($\bar{\bar{\chi}}_\mathrm{a}$). The slopes of the rays correspond to the refractive index $n_\mathrm{a,b}(\omega)$, with $n_\mathrm{a,b1,2}=n_\mathrm{a,b}(\omega_{1,2})$. The lower frequency (red) propagates faster than the higher frequency (blue). It is then refocused in medium 2, ($\bar{\bar{\chi}}_\mathrm{b}$), because the lower frequency is now faster than the higher frequency. It refocuses at position $z=2z_0$, where z_0 is the width of both media. The group delays of both media are related by:

$$\tau_\mathrm{a}(\omega,k_z)=\tau_\mathrm{b}(\omega_0-\omega,k_0-k_z), \tag{5.1}$$

where $\omega_0 = \omega_1 + \omega_2$. In Fig. 5.1 (a) we indeed find

$$\tau_{\mathrm{a}}(\omega_1) = \tau_{\mathrm{b}}(\omega_0 - \omega_1) = \tau_{\mathrm{b}}(\omega_2), \quad \tau_{\mathrm{a}}(\omega_2) = \tau_{\mathrm{b}}(\omega_1). \tag{5.2}$$

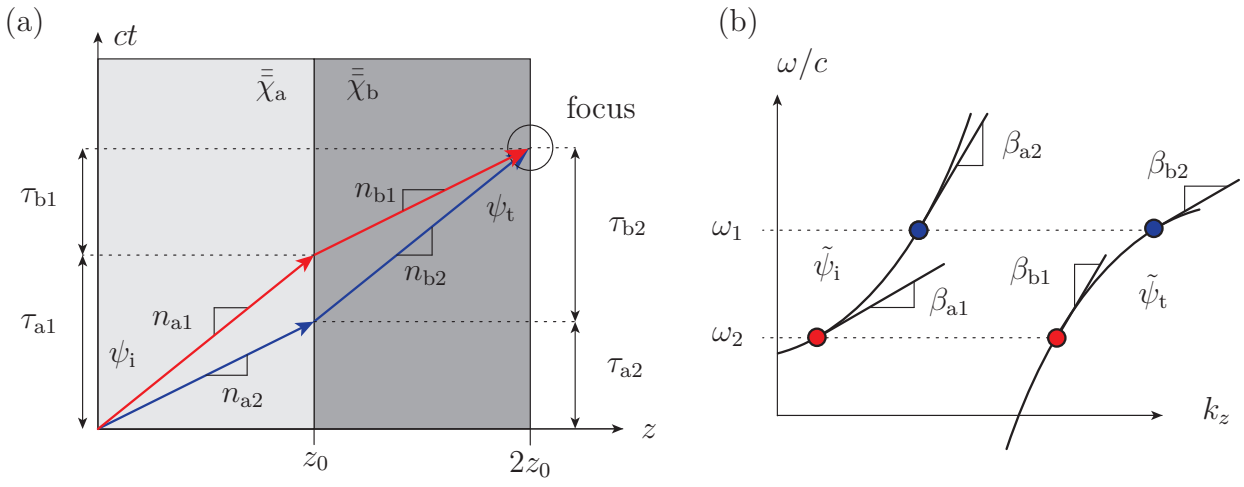

Figure 5.1 Illustration of focusing in transmission. (a) ST rays. (b) Qualitative dispersion diagram of the corresponding ST structure.

Notice how the curvatures of the dispersion diagrams are inversed. The dispersion of the first medium is concave, and the second is convex. This will also be the case for focusing in reflection, which is the next topic.

5.1.2 Focusing in Reflection

Compression in reflection is based on the same dispersion compensation principle, but there is only one medium, $\bar{\bar{\chi}}_{\mathrm{NR}}$, which is nonreciprocal, and so forward and backward propagating waves see different landscapes.

Figure 5.2(a) traces the ST trajectory of a pulse focused after reflection: it is first travelling to the right, and spreads out, with higher frequencies (blue) propagating *faster* than lower frequencies (red), given the dispersion (slope $\propto \partial\omega/\partial k_z = v_{\mathrm{g}}$, group velocity) of the medium shown in Fig. 5.2(b). After reflection, the velocities of the frequencies are inverted, due to the inversion of the dispersion curvatures, so that the higher frequencies are now propagating *slower* than the lower frequencies. Since the velocities are exactly opposite, focusing occurs at $z = 0$.

The dispersion curve for the backward wave shown in Fig. 5.2(b) is found by flipping the curve

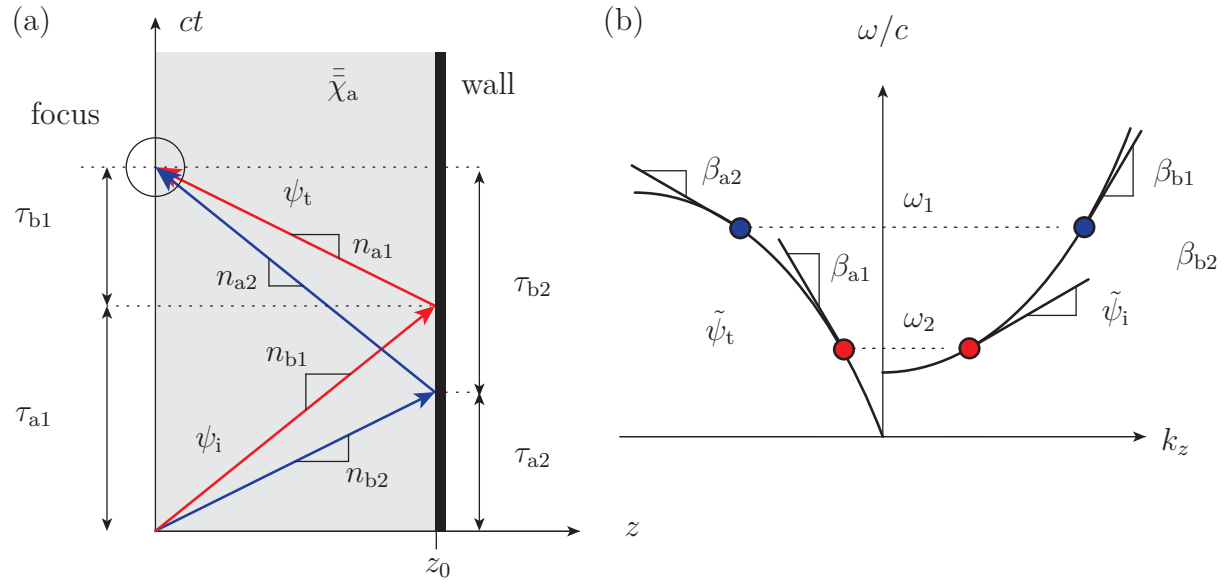

Figure 5.2 Illustration of focusing in reflection. (a) Minkowski representation. (b) Qualitative dispersion diagram of the corresponding ST structure.

of the forward dispersion around the k_z axis, and then translating the curve by $\omega_0 = \omega_1 + \omega_2$ such that the slope of the maximal (minimal) frequency of the incident wave is the inverse of the minimal (maximal) frequency of the reflected wave. Note that a medium with such an asymmetric dispersion with respect to the wavenumber is fundamentally a nonreciprocal one. The relation between the group delay for the medium seen by the incident wave and the reflected wave are related by:

$$\tau_{\mathrm{a}}(\omega, k_z) = \tau_{\mathrm{b}}(\omega_0 - \omega, k_z), \tag{5.3}$$

where $\omega_0 = \omega_1 + \omega_2$. This is consistent with the quantities indicated in Fig. 5.2 (a):

$$\tau_{\mathrm{a}}(\omega_1) = \tau_{\mathrm{b}}(\omega_2), \qquad \tau_{\mathrm{a}}(\omega_2) = \tau_{\mathrm{b}}(\omega_1). \tag{5.4}$$

5.1.3 STM Structure Realizing Focusing in Reflection

A subluminal dispersive crystal has the required dispersion slope to achieve compression in reflection. In particular, consider an ST-modulated collision-less plasma without magnetic

bias, whose wave equation reads

$$\left(\frac{\partial^2}{\partial z^2} - \frac{1}{c^2}\frac{\partial^2}{\partial t^2} - \frac{\omega_{\rm p}^2(z,t)}{c^2}\right)\mathbf{E} = 0, \tag{5.5}$$

with spatially periodic plasma frequency $\omega_{\rm p} = \omega_{\rm p0} + \Delta\omega_{\rm p}\cos(Kz - \Omega t)$ where K and Ω are the modulation wavenumber and frequency, respectively. Figure 5.3(a) represents such a medium in the Minkowski diagram. The wavelength and period of the medium are Λ and T, respectively, and the modulation velocity is therefore $v_{\rm m} = \Lambda/T$. A frame of reference moving along with the perturbation at velocity $v_{\rm m}$ sees only spatial periodicity. Therefore, the time axis ct' is drawn parallel to the interface of the ST modulation.

To mathematically derive the dispersion diagram corresponding to this medium, we first note that the solution of the wave equation (5.5) takes on the Bloch-Floquet form (Cassedy and Oliner, 1963):

$$\mathbf{E} = e^{i(kz-\omega t)}\sum_{m=-\infty}^{\infty}\mathbf{E}_m e^{im(Kz-\Omega t)}. \tag{5.6}$$

Inserting the expansion (5.6) into (5.5) yields a matrix equation whose determinant roots correspond to the dispersion diagram, schematically drawn in Fig. 5.3(b) for an infinitesimally small modulation $\Delta\omega_{\rm p} \to 0$. The temporal and spatial modulation frequencies are $\Omega = 2\pi/T$ and $K = 2\pi/\Lambda$, respectively. Notice the nonmodulated dispersion diagram corresponding to a single mode $m = 0$ is repeated along the spatial frequency axis k_z', since in that frame of reference the perturbation is spatial. The highlighted zones on the dispersion curves of Fig. 5.3(b) have opposite curvatures, as desired, and therefore focusing in reflection can occur.

5.2 Reverse Doppler Effect Explanation

The reversed Doppler effect corresponds to a frequency change that is opposite to that expected: an approaching boundary will scatter a downshifted wave. This was predicted to occur in negative index material by Veselago (Veselago, 1968). It was also shown to occur in periodic transmission lines, (Seddon and Bearpark, 2003) and in photonic crystals (Reed et al., 2003). Here, we suggest a diagrammatic explanation of the phenomena.

Figure 5.4(a) illustrates the STM structure that generates the reversed Doppler effect. Figure 5.4 (b) shows the STM structure in the Minkowski diagram. It consists of a periodic medium $\epsilon(z) = \epsilon(z + \zeta)$ bounded by a moving wall of velocity v. Figure 5.4 (c) shows the geometrical construction in the dispersion diagram leading to the scattered wave solutions, including the reversed Doppler effect. It is constructed using the following steps: 1) Draw

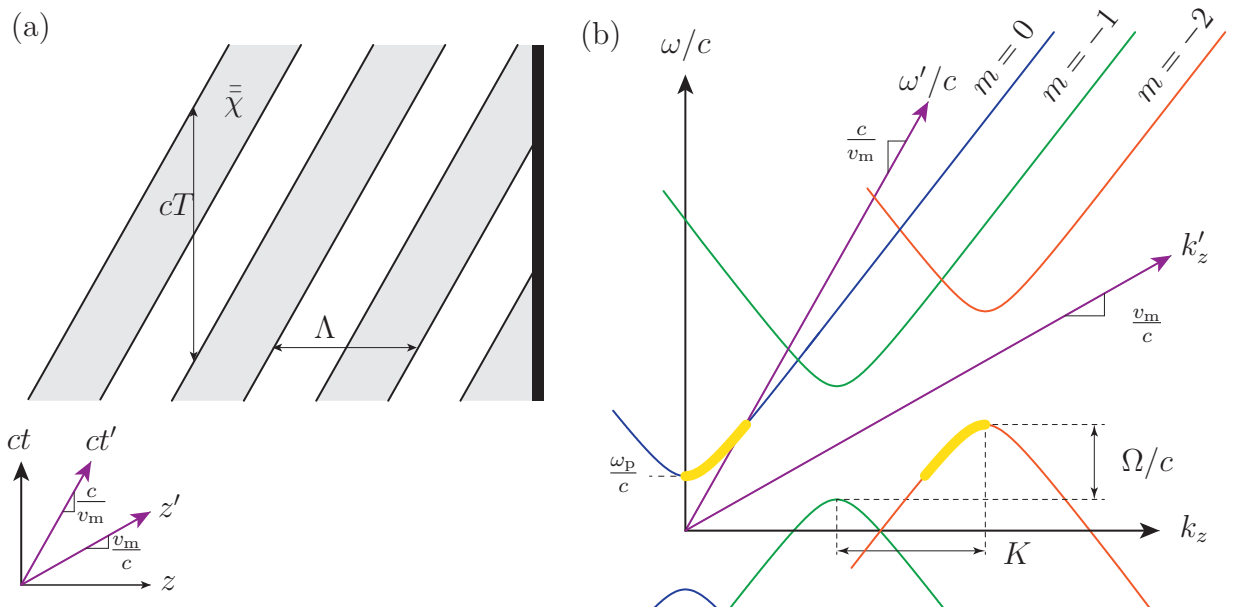

Figure 5.3 Subluminal crystal for focusing in reflection. (a) Minkwoski diagram representation. (b) Dispersion diagram, with required curvatures highlighted.

the dispersion diagram of a periodic stationary medium. 2) Draw the frequency axes for the stationary and the moving frames. 3) Locate the incident wave E_i. 4) Plot the isofrequency line in the moving frame ($\omega_\mathrm{i}' = \omega_\mathrm{r}'$), which is parallel to the k' axis.

Using this geometric construction, we immediately see the standard Doppler effect for the $E_{\mathrm{r}0}$ and the inverse Doppler shift for the E_{-1} solution. From the diagram, we find the equation for the temporal frequency harmonics:

$$\omega_n = \omega_i \frac{1-\beta}{1+\beta} + \frac{Kn}{1+\beta} \tag{5.7}$$

with $K = 2\pi/\Lambda$ the wavenumber of the modulation, and n the harmonic number. This corresponds to the results published in Reed et al. (2003). We see that for $m < 1$ the reflected frequency is less than the incident frequency, which corresponds to the reversed Doppler effect.

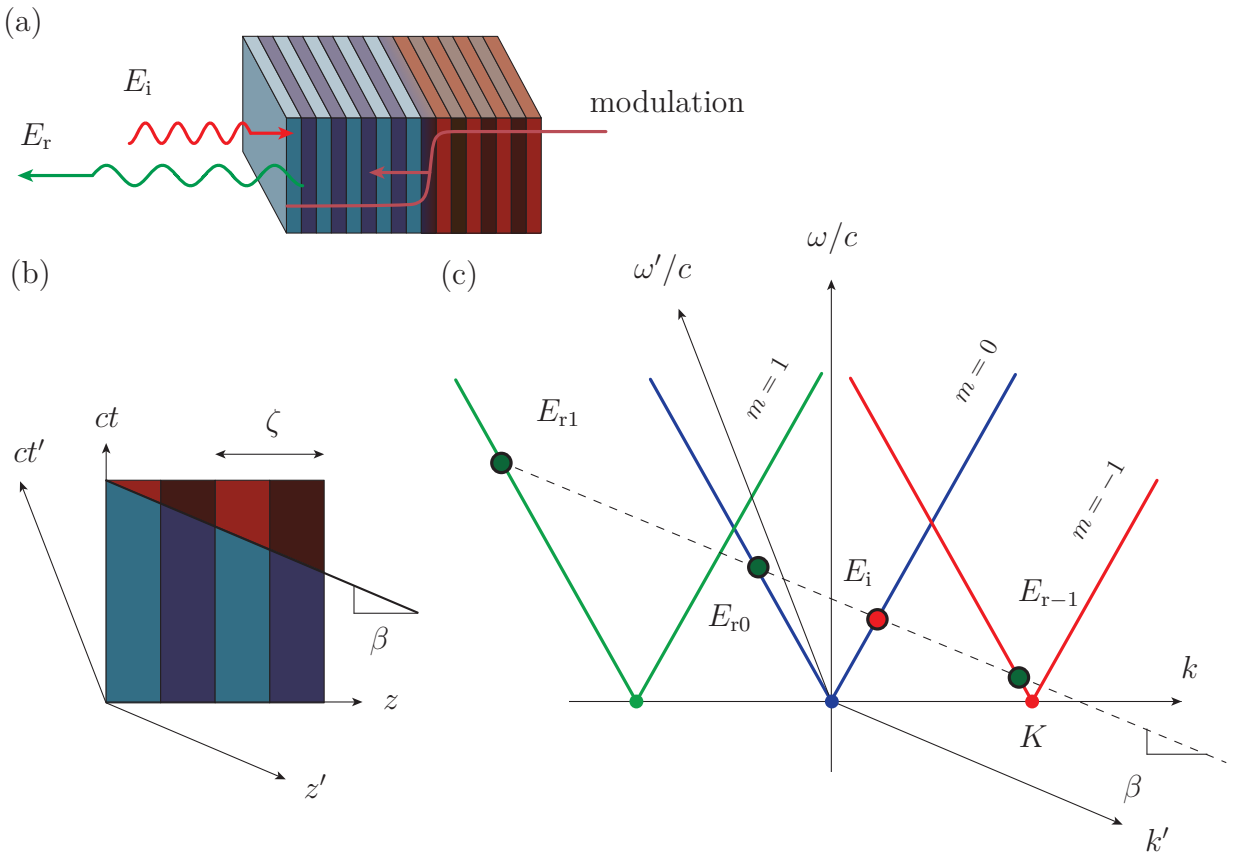

Figure 5.4 Inverse Doppler effect representation. (a) Illustration of the principle: a nonlinear stationnary crystal excited by a modulating wave, which creates a modulated moving discontinuity. (b) Representation in Minkowski diagram. (c) Dispersion diagram with incident wave, E_i, and reflected, E_{rm} solutions.

CHAPTER 6 CONCLUSION AND FUTURE WORKS

This work represents the beginning of our exploration of STM structures. The representation of STM structures in the Minkowski diagram and the classification of structures according to their spatial and temporal dependence gave us a global vision of STM structures, and brought us to identify several problems that have not been addressed.

Most of the thesis concentrates on two structures in particular, the superluminal slab and the superluminal crystal. They were studied using a diagrammatic method applicable to all linear-motion problems. This diagrammatic methodology, combining STM media representations in Minkowski diagrams and Lorentz transformations, helped us solve the problem of the superluminal slab, led to the discovery of a surprising symmetry between subluminal and superluminal slabs, and led to the understanding of interference patterns in superluminal slabs. Therefore the methodology proved to be an effective and versatile tool. However it is limited to linear motion STM structures, as the Lorentz transformation applies to frames moving at constant velocities. It is also limited to anisotropic media, since the dispersion diagrams cannot represent the coupling between electric and magnetic fields.

A few future projects are planned. First of all the analysis of the superluminal crystal will be completed. A more complete and rigorous approach to the instability conditions, based on the Sylvester theorem, is planned. The work on the focusing structure presented in Chapter 4 will also be completed by numerical and experimental studies.

An interesting and important problem we would like to tackle is the synthesis of STM non-periodic structures. Indeed, all the periodic structures we studied give rise to unwanted harmonics, which could be avoided if the structures were aperiodic. A synthesis tool would enable us to design a great variety of STM structures. The future steps in this direction would be to choose a standard filter synthesis tool, and try to extend it to temporal variation, before going to STM variation.

REFERENCES

S. Abielmona, S. Gupta, et C. Caloz, "Compressive receiver using a CRLH-based dispersive delay line for analog signal processing", *IEEE Trans. Microw. Theory Tech.*, vol. 57, no. 11, pp. 2617–2626, 2009.

V. Bacot, M. Labousse, A. Eddi, M. Fink, et E. Fort, "Time reversal and holography with spacetime transformations", *Nat. Phys.*, vol. 12, pp. 972–977, 2016.

F. Biancalana, A. Amann, A. V. Uskov, et E. P. O'Reilly, "Dynamics of light propagation in spatiotemporal dielectric structures", *Phys. Rev. E*, vol. 75, no. 4, p. 046607, 2007.

E. S. Cassedy, "Dispersion relations in time-space periodic media: Part II-Unstable interactions", *Proc. IEEE*, vol. 55, no. 7, pp. 1154–1168, 1967.

E. S. Cassedy et A. A. Oliner, "Dispersion relations in time-space periodic media: Part I-Stable interactions", *Proc. IEEE*, vol. 51, no. 10, pp. 1342–1359, 1963.

N. Chamanara, S. Taravati, Z.-L. Deck-Léger, et C. Caloz, "Optical isolation based on space-time engineered asymmetric photonic bandgaps", *arXiv:1612.08398*, 2016.

R.-S. Chu et T. Tamir, "Guided-wave theory of light diffraction by acoustic microwaves", *IEEE Trans. Microw. Theory Tech.*, vol. 119, no. 11, pp. 487–504, 1969.

R. E. Collins, *Field Theory of Guided Waves, Second Edition*. Wiley, 1991, Ch. 3.

A. L. Cullen, "A traveling-wave parametric amplifier", *Nature*, vol. 181, no. 4605, pp. 332–332, 1958.

Z.-L. Deck-Léger et C. Caloz, "Wave scattering by superluminal space-time modulated slabs and symmetries with the subluminal case", *arXiv:1611.01366*, 2016.

——, "Scattering in superluminal space-time (ST) modulated electromagnetic crystals", dans *IEEE AP-S Int. Antennas Propag.*, San Diego, California, USA, Jul. 2017.

——, "Space-time (st) reflection focusing in dispersion-engineered medium", dans *URSI General Assembly and Scientific Symposium (GASS)*, Montreal, Canada, Aug. 2017.

N. A. Estep, D. L. Sounas, J. Soric, et A. Alù, "Magnetic-free non-reciprocity and isolation based on parametrically modulated coupled-resonator loops", *Nature Phys.*, vol. 10, no. 12, pp. 923–927, 2014.

R. L. Fante, "Transmission of electromagnetic waves into time-varying media", *Antennas and Propagation, IEEE Transactions on*, vol. 19, no. 3, pp. 417–424, 1971.

L. Felsen et G. M. Whitman, "Wave propagation in time-varying media", *IEEE Trans. Antennas. Propag.*, vol. 18, no. 2, pp. 242–253, 1970.

H. Fizeau, "Sur les hypothèses relatives à l'éther lumineux, et sur une expérience qui parait démontrer que le mouvement des corps change la vitesse avec laquelle la lumière se propage dans leur intérieur", *C.R. Acad. Sci.*, vol. 33, p. 349, 1851.

M. Fridman, A. Farsi, Y. Okawachi, et A. L. Gaeta, "Demonstration of temporal cloaking", *Nature Lett.*, vol. 481, pp. 62–65, 2012.

D. Holberg et K. Kunz, "Parametric properties of fields in a slab of time-varying permittivity", *IEEE Trans. Antennas. Propag.*, vol. 14, no. 2, pp. 183–194, 1966.

J. D. Jackson, *Electrodynamics*. Wiley Online Library, 1975.

A. B. Kozyrev et D. W. van der Weide, "Reply to comment on "explanation of the inverse Doppler effect observed in nonlinear transmission lines"", *Phys. Rev. Lett.*, vol. 96, p. 069403, 2006.

——, "Explanation of the inverse Doppler effect observed in nonlinear transmission lines", *Phys. Rev. Lett.*, vol. 94, p. 203902, 2005.

K. S. Kunz, "Plane electromagnetic waves in moving media and reflections from moving interfaces", *J. Appl. Phys.*, vol. 51, no. 2, pp. 873–884, 1980.

K. A. Lurie et S. L. Weekes, "Wave propagation and energy exchange in a spatio-temporal material composite with rectangular microstructure", *J. Math. Anal. Appl.*, vol. 314, pp. 286–310, 2006.

K. A. Lurie et V. V. Yakolev, "Energy accumulation in waves propagating in space- and time-varying transmission lines", *IEEE Antenn. Wireless Propag. Lett.*, vol. 15, pp. 1681–1684, 2016.

M. W. McCall, A. Favaro, P. Kinsler, et A. Boardman, “A spacetime cloak, or a history editor”, *J. Opt*, vol. 13, p. 024003, 2011.

H. Minkowski, “Raum und Zeit”, *Jahresbericht der Deutschen Mathematiker-Vereinigung*, vol. 18, pp. 75–88, 1909.

F. R. Morgenthaler, “Velocity modulation of electromagnetic waves”, *IEEE Trans. Microw. Theory Techn.*, vol. 6, no. 2, pp. 167–172, 1958.

J. R. Pierce, “Use of the principles of conservation of energy and momentum in connection with the operation of wave-type parametric amplifiers”, *J. Appl. Phys.*, vol. 30, no. 9, pp. 1341–1346, 1958.

J. Ran, Y. Zhang, X. Chen, K. Fang, J. Zhao, Y. Sun, et H. Chen, “Realizing tunable inverse and normal doppler shifts in reconfigurable rf metamaterials”, *Scientific reports*, vol. 5, 2015.

E. J. Reed, M. Soljačić, et J. D. Joannopoulos, “Color of shock waves in photonic crystals”, *Phys. Rev. Lett.*, vol. 90, no. 20, p. 203904, 2003.

E. J. Reed, M. Soljačić, M. Ibanescu, et J. D. Joannopoulos, “Comment on "Observation of the inverse Doppler effect"”, *Science*, vol. 305, p. 778, 2004.

E. J. Rothwell et M. J. Cloud, *Electromagnetics, Second Edition*. CRC Press, 2009.

B. E. A. Saleh et M. C. Teich, *Fundamentals of Photonics*. Wiley, 2007, Chap. 19, 21.

M. A. Salem et C. Caloz, “Wave propagation in periodic temporal slabs”, dans *2015 9th European Conference on Antennas and Propagation (EuCAP)*. IEEE, 2015, pp. 1–2.

N. Seddon et T. Bearpark, “Observation of the inverse Doppler effect”, *Science*, vol. 302, pp. 1537–1540, 2003.

——, “Response to comment on "Observation of the inverse Doppler effect"”, *Science*, vol. 305, p. 778, 2004.

A. Shaltout, A. Kildishev, et V. Shalaev, “Time-varying metasurfaces and Lorentz non-reciprocity”, *Optical Materials Express*, vol. 5, no. 11, pp. 2459–2467, 2015.

Y. Sivan et J. B. Pendry, “Time reversal in dynamically tuned zero-gap periodic systems”, *Phys. Rev. Lett.*, vol. 106, no. 19, p. 193902, 2011.

M. Skorobogatiy et J. D. Joannopoulos, “Photon modes in photonic crystals undergoing rigid vibrations and rotations”, *Phys. Rev. B.*, vol. 61, no. 23, p. 15554, 2000.

——, “Rigid vibrations of a photonic crystal and induced interband transitions”, *Phys. Rev. B.*, vol. 61, no. 8, p. 5293, 2000.

D. L. Sounas, C. Caloz, et A. Alù, “Giant non-reciprocity at the subwavelength scale using angular momentum-biased metamaterials”, *Nat. Commun.*, vol. 4, 2013.

J. Strutt, “On the maintenance of vibrations by forces of double frequency, and on the propagation of waves through a medium endowed with a periodic structure”, *Phil. Mag.*, vol. 24, no. 147, pp. 145–159, 1887.

T. Tamir et H. C. Wang, “Scattering of electromagnetic waves by a sinusoidally stratified half-space. I. Formal solution and analytic approxiamtions”, *Canadian Journal of Physics*, vol. 44, pp. 167–172, 1966.

S. Taravati et C. Caloz, “Mixer-duplexer-antenna leaky-wave system based on periodic space-time modulation”, *IEEE Trans. Antennas Propag*, vol. 65, no. 2, pp. 442–452, 2017.

P. K. Tien, “Parametric amplification and frequency mixing in propagating circuits”, *J. Appl. Phys.*, vol. 29, no. 9, pp. 1347–1357, 1958.

V. G. Veselago, “The electrodynamics of substances with simultaneously negative values of ϵ and μ”, *Soviet Physics Uspekhi*, vol. 10, no. 4, pp. 509–514, 1968.

E. Yablonovitch, “Inhibited spontaneous emission in solid-state physics and electronics”, *Phys. Rev. Lett.*, vol. 58, no. 20, p. 2059, 1987.

C. Yeh et K. F. Casey, “Reflection and transmission of electromagnetic waves by a moving dielectric slab”, *Phys. Rev.*, vol. 144, pp. 665–669, 1966.

Z. Yu et S. Fan, “Complete optical isolation created by indirect interband photonic transitions”, *Nat. Photon.*, vol. 3, no. 2, pp. 91–94, 2009.

J. R. Zurita-Sánchez, P. Halevi, et J. C. Cervantes-Gonzalez, "Reflection and transmission of a wave incident on a slab with a time-periodic dielectric function ε (t)", *Physical Review A*, vol. 79, no. 5, p. 053821, 2009.

APPENDIX A Scattering from a Subluminal Slab

Here we calculate the scattering coefficients for a wave normally incident on a subluminal slab, to compare the results with those from a superluminal slab.

We first start by solving the half-space problem. Consider two media of refractive indices n_1 and n_2. The continuity conditions at the interface of a modulated subluminal half-space are expressed in the moving frame as:

$$\left[E'^{+}_{y_1} + E'^{-}_{y_1} = E'^{+}_{y_2}\right]_{z'=0} \tag{A.1a}$$

$$\left[H'^{+}_{x_1} + H'^{-}_{x_1} = H'^{+}_{x_2}\right]_{z'=0} \tag{A.1b}$$

and the propagation constants found using phase matching and Lorentz transforms:

$$k_{z1}^{+\prime} = k_{z1}^{-\prime} = k_{z2}^{+\prime} \tag{A.2a}$$

$$k_{z1}^{+}(1-\beta n_1) = k_{z1}^{-}(1+\beta n_1) = k_{z2}^{+}(1-\beta n_2) \tag{A.2b}$$

from this, we can deduce the temporal frequencies:

$$\omega_1^{+}\frac{1-\beta n_1}{n_1} = \omega_1^{-}\frac{1+\beta n_1}{n_1} = \omega_2^{+}\frac{1-\beta n_2}{n_2}. \tag{A.2c}$$

The Lorentz transformations are:

$$cE'_x = \gamma\left(E_x + c\beta B_y\right), \quad cH'_y = \gamma\left(H_y + c\beta D_x\right). \tag{A.3}$$

inserting these into (A.1) yields

$$E^{+}_{y_{1,1}} + \beta cB^{+}_{x_{1,1}} + E^{-}_{y_{1,1}} + \beta cB^{-}_{x_{1,1}} = E^{+}_{y_{2,1}} + \beta cB^{+}_{x_{2,1}} \tag{A.4}$$

$$H^{+}_{x_{1,1}} + \beta cD^{+}_{y_{1,1}} + H^{-}_{x_{1,1}} + \beta cD^{-}_{y_{1,1}} = H^{+}_{x_{2,1}} + \beta cD^{+}_{y_{2,1}} \tag{A.5}$$

considering a harmonic wave $E_1^+ = A_1^+ e^{i(\omega_1^+ t - k_{z1}^+ z)}$, and applying Maxwell's equations yields

$$A_1^+(1-\beta n_1) + A_1^-(1+\beta n_1) = A_2^+(1-\beta n_2) \tag{A.6a}$$

$$A_1^+(1-\beta n_1) - A_1^-(1+\beta n_1) = \frac{\eta_1}{\eta_2} A_2^+(1-\beta n_2) \tag{A.6b}$$

This system of equations yields

$$\rho_1^+ = \frac{A_1^-}{A_1^+} = \frac{(\eta_2-\eta_1)(1-\beta n_1)}{(\eta_1+\eta_2)(1+\beta n_1)} \tag{A.7a}$$

$$\tau_1^+ = \frac{A_2^-}{A_1^+} = \frac{(2\eta_2)(1-\beta n_1)}{(\eta_1+\eta_2)(1-\beta n_2)} \tag{A.7b}$$

where the positive superscript refers to the direction of the incident wave, in this case it is in the $+z$ direction. The scattering coefficients for an incident wave moving in the $-z$ direction are found by changing the sign of the velocity of the slab. The coefficients for a wave in medium of refractive index n_2 incident on a half-space of refractive index n_1 is found by switching the refractive indices in (A.7).

We now want to solve the scattering from a slab. This is realized by using matching matrices and propagation matrices, as shown in Collins (1991). The following equations relate the fields in the first medium to the fields inside the slab, at the position of the first interface.

$$E_{2,1}^+ = \tau_{12}^+ E_{1,1}^+ + \rho_2^- E_{2,1}^- \tag{A.8a}$$

$$E_{1,1}^- = \rho_1^+ E_{1,1}^+ + \tau_{21}^- E_{2,1}^- \tag{A.8b}$$

where the field $E_{m,n}$ corresponds to the field in medium m at the interface n, as seen in Fig. A.1, and $\tau_{ij}^{\pm}$, $\rho_{ij}^{\pm}$ correspond to transmission and reflection coefficients from medium i to medium j, and the $+,-$ superscript correspond to incident waves propagating in the $\pm z$ direction.

Equations (A.8) may be written in matrix form

$$\begin{bmatrix} E_{1,1}^+ \\ E_{1,1}^- \end{bmatrix} = \frac{1}{\tau_{12^+}} \begin{bmatrix} 1 & -\rho_2^- \\ \rho_1^+ & \tau_{12}^+\tau_{21}^- - \rho_1^+\rho_2^- \end{bmatrix} \begin{bmatrix} E_{2,1}^+ \\ E_{2,1}^- \end{bmatrix} \tag{A.9}$$

The propagation matrix relates the fields inside the slab from one interface to the other. The equations are:

$$E_{2,2}^+ = E_{2,1}^+ e^{i\phi^+}, \tag{A.10a}$$

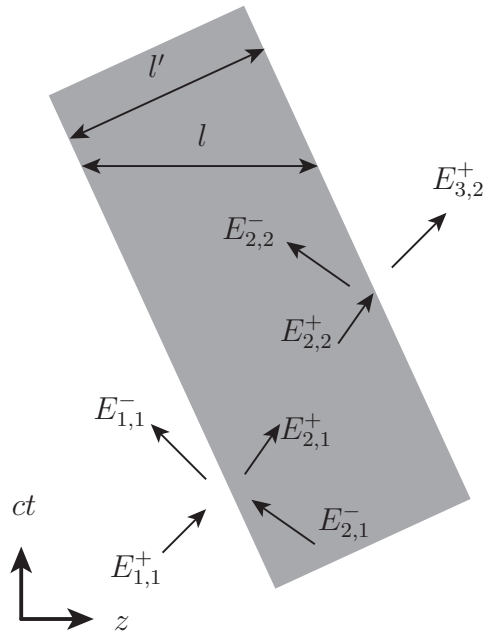

Figure A.1 Definition of fields for subluminal slab calculations

$$E^-_{2,1} = E^-_{2,2} e^{i\phi^-}, \tag{A.10b}$$

where the phase $\phi^\pm = k^\pm_{z2} l$. We find the matrix:

$$\begin{bmatrix} E^+_{2,1} \\ E^-_{2,2} \end{bmatrix} = \begin{bmatrix} e^{-i\phi^+} & 0 \\ 0 & e^{i\phi^-} \end{bmatrix} \begin{bmatrix} E^+_{2,2} \\ E^-_{2,1} \end{bmatrix}. \tag{A.11}$$

The following equations relate the fields in the slab at the second interface to the fields transmitted through the slab:

$$E^+_{3,2} = \tau^+_{21} \bar{E}^+_{2,2}, \tag{A.12a}$$

$$E^-_{2,2} = \rho^+_2 E^+_{2,2}. \tag{A.12b}$$

(A.12) is written in matrix form as

$$\begin{bmatrix} E^+_{2,2} \\ E^-_{2,2} \end{bmatrix} = \frac{1}{\tau_{21^+}} \begin{bmatrix} 1 & -\rho^-_1 \\ \rho^+_2 & \tau^-_{12}\tau^+_{21} - \rho^-_1 \rho^+_2 \end{bmatrix} \begin{bmatrix} E^+_{3,2} \\ 0 \end{bmatrix}. \tag{A.13}$$

Finally, cascading the matrices yields

$$\begin{bmatrix} E^+_{1,1} \\ E^-_{1,1} \end{bmatrix} = \frac{1}{\tau^+_{21}\tau^+_{12}} \begin{bmatrix} 1 & -\rho^-_2 \\ \rho^+_1 & \tau^+_{12}\tau^-_{21} - \rho^+_1\rho^-_2 \end{bmatrix} \begin{bmatrix} e^{-i\phi^+} & 0 \\ 0 & e^{i\phi^-} \end{bmatrix} \begin{bmatrix} 1 & -\rho^-_1 \\ \rho^+_2 & \tau^+_{21}\tau^-_{12} - \rho^+_2\rho^-_1 \end{bmatrix} \begin{bmatrix} E^+_{3,2} \\ 0 \end{bmatrix}, \quad \text{(A.14)}$$

from which we derive the reflection and transmission coefficients

$$T = \frac{E^+_{3,2}}{E^+_{1,1}} = \frac{\tau^+_{21}\tau^+_{12}}{e^{-i\phi^+} - \rho^-_2\rho^+_2 e^{i\phi^-}} = \frac{\tau^+_{21}\tau^+_{12}e^{i\phi^+}}{1 - \rho^-_2\rho^+_2 e^{i(\phi^+ + \phi^-)}}, \quad \text{(A.15a)}$$

$$\Gamma = \frac{E^-_{1,1}}{E^+_{1,1}} = \frac{\rho^+_1 + (\tau^+_{12}\tau^-_{21} - \rho^+_1\rho^-_2)\rho^+_2 e^{i(\phi^+ + \phi^-)}}{1 - \rho^-_2\rho^+_2 e^{i(\phi^+ + \phi^-)}}. \quad \text{(A.15b)}$$